

ASTEROSEISMOLOGY OF 16000 *Kepler* RED GIANTS: GLOBAL OSCILLATION PARAMETERS, MASSES, AND RADII

JIE YU,^{1,2} DANIEL HUBER,^{3,1,4,2} TIMOTHY R. BEDDING,^{1,2} DENNIS STELLO,^{5,1,2} MARC HON,⁵ SIMON J. MURPHY,^{1,2} AND
 SHOURYA KHANNA¹

¹ Sydney Institute for Astronomy (SIfA), School of Physics, University of Sydney, NSW 2006, Australia

² Stellar Astrophysics Centre, Department of Physics and Astronomy, Aarhus University, Ny Munkegade 120, DK-8000 Aarhus C, Denmark

³ Institute for Astronomy, University of Hawai‘i, 2680 Woodlawn Drive, Honolulu, HI 96822, USA

⁴ SETI Institute, 189 Bernardo Avenue, Mountain View, CA 94043, USA

⁵ School of Physics, University of New South Wales, NSW 2052, Australia

ABSTRACT

The *Kepler* mission has provided exquisite data to perform an ensemble asteroseismic analysis on evolved stars. In this work we systematically characterize solar-like oscillations and granulation for 16,094 oscillating red giants, using end-of-mission long-cadence data. We produced a homogeneous catalog of the frequency of maximum power (typical uncertainty $\sigma_{\nu_{\max}}=1.6\%$), the mean large frequency separation ($\sigma_{\Delta\nu}=0.6\%$), oscillation amplitude ($\sigma_A=4.7\%$), granulation power ($\sigma_{\text{gran}}=8.6\%$), power excess width ($\sigma_{\text{width}}=8.8\%$), seismically-derived stellar mass ($\sigma_M=7.8\%$), radius ($\sigma_R=2.9\%$), and thus surface gravity ($\sigma_{\log g}=0.01$ dex). Thanks to the large red giant sample, we confirm that red-giant-branch (RGB) and helium-core-burning (HeB) stars collectively differ in the distribution of oscillation amplitude, granulation power, and width of power excess, which is mainly due to the mass difference. The distribution of oscillation amplitudes shows an extremely sharp upper edge at fixed ν_{\max} , which might hold clues to understand the excitation and damping mechanisms of the oscillation modes. We find both oscillation amplitude and granulation power depend on metallicity, causing a spread of 15% in oscillation amplitudes and a spread of 25% in granulation power from $[\text{Fe}/\text{H}]=-0.7$ to 0.5 dex. Our asteroseismic stellar properties can be used as reliable distance indicators and age proxies for mapping and dating galactic stellar populations observed by *Kepler*. They will also provide an excellent opportunity to test asteroseismology using Gaia parallaxes, and lift degeneracies in deriving atmospheric parameters in large spectroscopic surveys such as APOGEE and LAMOST.

Keywords: catalogs: fundamental parameters — stars: late-type — techniques: photometric

1. INTRODUCTION

Red giants are bright, cool and evolved stars which oscillate with amplitudes ranging from a few tens to thousands of parts per million and with characteristic oscillation timescales varying from hours up to months (De Ridder et al. 2009; Huber et al. 2011a; Mosser et al. 2012a; Stello et al. 2014). Out of more than 196,000 stars observed by the *Kepler* space telescope (Borucki et al. 2010; Koch et al. 2010), some 19,000 oscillating red giants have so far been detected (Hekker et al. 2011a; Huber et al. 2011a; Stello et al. 2013; Huber et al. 2014; Mathur et al. 2016; Yu et al. 2016). The study of solar-like oscillations in giants has led to a number of breakthrough discoveries such as classification of the evolutionary stages of red giants (Bedding et al. 2011; Mosser et al. 2012b; Stello et al. 2013; Mosser et al. 2015; Vrard et al. 2016; Elsworth et al. 2017; Hon et al. 2017), measurement of internal rotation (Beck et al. 2012; Deheuvels et al. 2012; Mosser et al. 2012b; Deheuvels et al. 2014) and possible detection of magnetic fields in radiative cores (Fuller et al. 2015; Stello et al. 2016; Mosser et al. 2017). It has also provided an excellent opportunity to implement Galactic archeology (Miglio et al. 2013; Stello et al. 2015; Casagrande et al. 2016; Sharma et al. 2016) and to characterize exoplanet properties (Huber et al. 2013a; Quinn et al. 2015).

Prior to the *Kepler* mission, some analyses focusing on the seismic determination of stellar mass and radius have been presented, for example by Gilliland (2008) and Stello & Gilliland (2009), who investigated the time series collected by the Hubble Space Telescope; by Stello et al. (2008), who worked with the star tracker of WIRE satellite; and by Kallinger et al. (2010a) and Mosser et al. (2010), who used data from the CoRoT telescope (Michel et al. 2008). Similar work has been done to derive the stellar properties for oscillating red giants observed by *Kepler*, but only focusing on exoplanet host stars (Huber et al. 2013b) or using short datasets (Kallinger et al. 2010b; Hekker et al. 2011a). This motivates us to study oscillations in red giants using the full four years of *Kepler* data, aiming at providing a large and homogeneous catalog of seismic masses and radii.

In order to determine stellar fundamental properties of red giants, three methods are widely used: the so-called direct method (Hekker et al. 2011a), grid-based modeling (Stello & Gilliland 2009; Kallinger et al. 2010b; Huber et al. 2013b; Chaplin et al. 2014b) and individual frequency modeling (Kallinger et al. 2008; di Mauro et al. 2011; Deheuvels et al. 2012; Quinn et al. 2015; Di Mauro et al. 2016; Li et al. 2018). Under the grid-based modeling method, atmospheric parameters and global seismic parameters are usually fitted to a grid of isochrones,

which inevitably hold some model dependencies. This technique is efficient for main-sequence stars and subgiants but calls for additional efforts to have their evolutionary phases distinguished for red giants since their evolutionary tracks converge in the Hertzsprung-Russell (H-R) diagram. The individual frequency analysis allows the investigation of mass, age, and internal physical processes, such as overshooting and transport of angular momentum. But it rests on unambiguous identifications of a series of frequencies, which is only possible for high signal-to-noise ratio photometric time series. Furthermore, it is time-consuming to model individual frequencies for tens of thousands of red giants. The direct method makes use of seismic scaling relations, possibly with associated corrections, to efficiently determine stellar parameters. It has been tested theoretically and observationally, with a typical accuracy of $\sim 5\%$ and $\sim 10\text{--}15\%$ in radius and mass for red giants, respectively (Silva Aguirre et al. 2012; Brogaard et al. 2012; Huber et al. 2012; Miglio 2012; White et al. 2013; Gaulme et al. 2016; Huber et al. 2017). We adopted the direct method to infer stellar fundamental properties in this work.

The primary goal of this work is to construct a large homogeneous catalog of global oscillation and granulation parameters and asteroseismic stellar masses, radii, and surface gravities for *Kepler* oscillating red giants. We also attempt to investigate the mass and metallicity influence on oscillation amplitude, granulation power, and width of power excess. For this we use full-mission *Kepler* data. Our sample consists of 16,094 *Kepler* red-giant oscillators, representing the largest known sample so far to homogeneously perform an ensemble asteroseismic analysis.

2. SAMPLE SELECTION AND DATA ANALYSIS

Kepler data are divided into quarters with a 10-d commissioning run, followed by the first 33-d quarter and subsequent 90-d regular quarters. In this work we make use of simple aperture photometry data collected in long-cadence mode. Figure 1 illustrates the histogram of duration of the long-cadence time series and the distribution of *Kepler* magnitudes of our sample.

Our sample is comprised of the known oscillating red giants from six published samples, as shown in the Venn diagram Figure 2. Some key properties of those six samples are summarized as follows:

- Hekker et al. (2011a) conducted an asteroseismic characterization of over 16,000 red giants. For 10,956 red giants, oscillations were detected and stellar fundamental parameters were derived using the data recorded in the first quarter (Q1) of *Kepler* data.

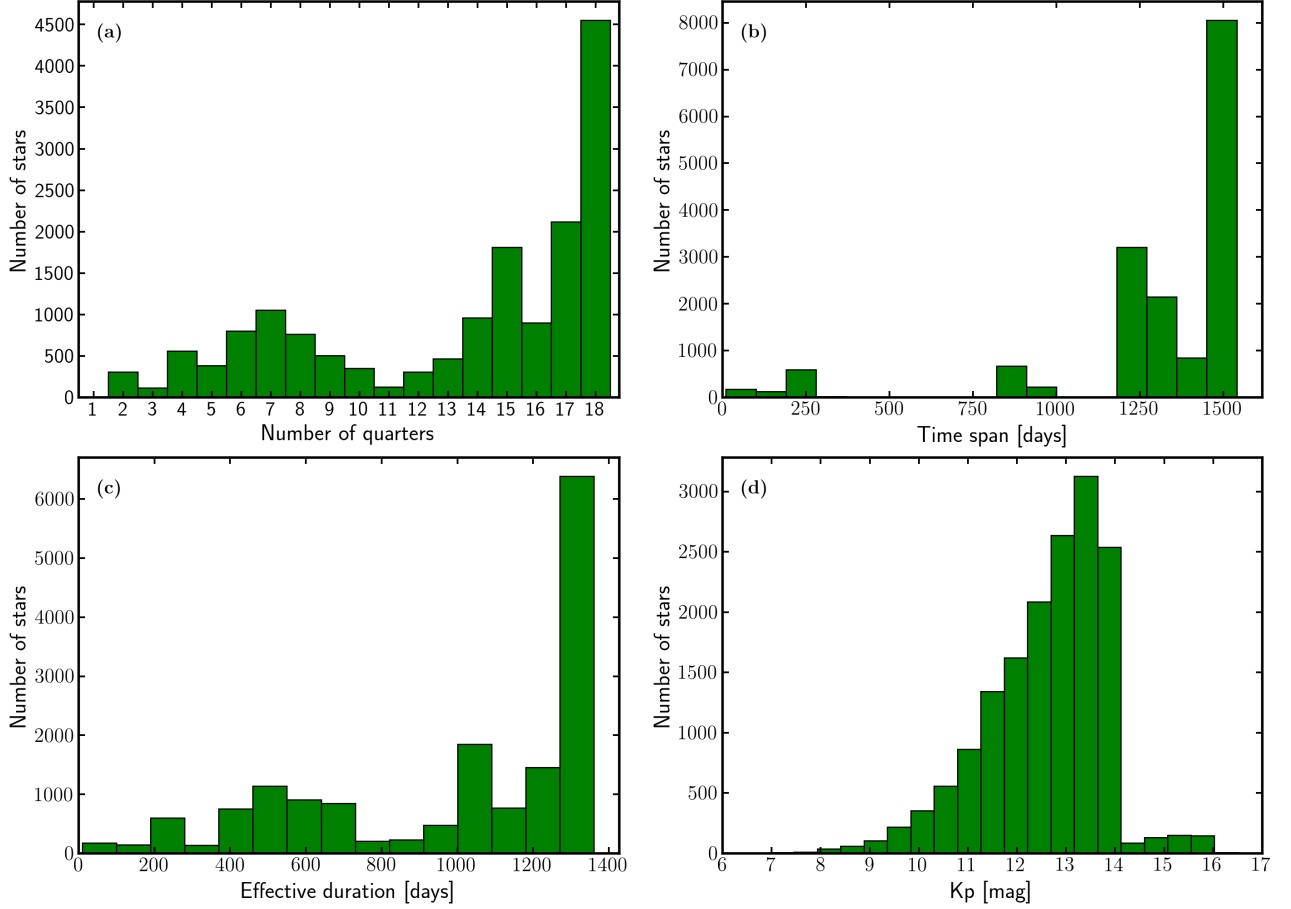


Figure 1. Distributions of time series length, including Q0 through Q17, and *Kepler* magnitude for our entire sample of 16,094 oscillating red giants. (a) number of quarters, (b) time span, (c) effective duration (number of data points times the integration time of 29.4 min), and (d) *Kepler* magnitude. The significant difference between panels (a) and (b) is due to some stars having big gaps in the time series.

- Huber et al. (2011a) used a sample of 1686 *Kepler* targets consisting of dwarfs and giants to test seismic scaling relations using long-cadence data spanning from Q0 to Q6 and short-cadence data from Q0 to Q4.
- Stello et al. (2013) detected solar-like oscillations in 13,412 red giants, with the aim of classifying evolutionary phase by measuring period spacing of dipole modes identified with long-cadence datasets from Q0 through Q8.
- Huber et al. (2014) presented a revised stellar properties catalog for 196,468 *Kepler* targets, and detected oscillations in 3114 stars that were unclassified in the *Kepler* Input Catalog (KIC, Brown et al. 2011). For this sample, only the frequency of maximum oscillation power, ν_{\max} , was measured.

- Mathur et al. (2016) discovered solar-like oscillations in over 800 faint and distant red giants misclassified as dwarfs by the KIC.
- Yu et al. (2016) distinguished the real oscillation power excess from the aliased one in the power density spectrum and discovered 626 new oscillating red giants that had been misclassified as subgiants in the KIC.

We excluded red giants with $\nu_{\max} < 5 \mu\text{Hz}$, resulting in a sample with $\log g \gtrsim 1.5$ dex and luminosity $\log(L/L\odot) \lesssim 2.24$ dex. Those excluded stars are expected to show oscillations in a few low radial-order acoustic modes (Stello et al. 2014). The seismic mass and radius inferred from scaling relations are likely to be biased for such star, as the scaling relations used are based on the asymptotic theory (Tassoul 1980; Gough 1986). We also removed dwarfs, subgiants, and stars with $\nu_{\max} > 275 \mu\text{Hz}$ due to the difficulty of fitting their power spectrum background. After visual inspection on

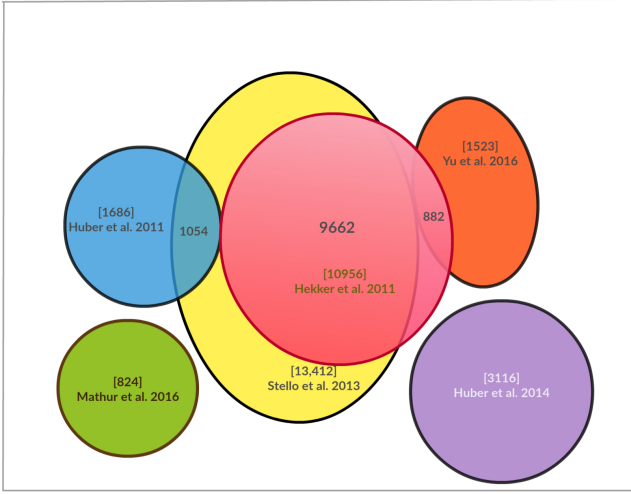


Figure 2. Sample selection. The oscillating red giants constituting our entire sample are collected from six samples. The numbers in the square brackets show the original number of stars in the corresponding source, while the unbracketed numbers indicate the number of common stars in two overlapping samples. For clarity, overlaps of ≤ 50 stars are not shown. There are 16,094 oscillating red giants from these known samples constituting our entire sample, after applying a cut $5\mu\text{Hz} < \nu_{\max} < 275\mu\text{Hz}$ and removing false and marginal detections.

our results, we removed outliers arising from wrong detections (non-oscillators) or marginal detections due to low signal-to-noise ratios. In the case where a star was analyzed in multiple literature samples, we adopted the one from the sample using the longest time series. Our final sample thus includes 133 stars from Hekker et al. (2011a), 336 stars from Huber et al. (2011a), 12975 stars from Stello et al. (2013), 705 stars from Huber et al. (2014), 606 stars from Mathur et al. (2016), and 1339 stars from Yu et al. (2016). This sample comprises 16,094 oscillating red giants.

We corrected instrumental trends following the method described by García et al. (2011). Long-cadence light curves were stitched together, with safe-mode events removed and jumps corrected using a linear fit. A quadratic Savitzky-Golay high-pass filter was applied to remove instrument variability and low-frequency signals arising from stellar activity. We used an adaptive smoothing width, d , as a linear function of ν_{\max} (taken from the literature), following $d = 0.61 + 0.04\nu_{\max}$. Thus the smoothing width varied from $0.8\mu\text{Hz}$ to $13.5\mu\text{Hz}$ when ν_{\max} increased from $5\mu\text{Hz}$ to the Nyquist frequency. A 4σ -clipping was applied to remove outliers from the high-pass filtered light curves.

The granulation and seismic parameters extracted in this work are the frequency of maximum oscillation

power (ν_{\max}), the mean frequency separation of acoustic modes with the same angular degree and consecutive radial order ($\Delta\nu$), the oscillation amplitude per radial mode (A), the width of the power excess hump characterized by a Gaussian envelope, and granulation power measured at ν_{\max} . Specifically, the oscillation amplitude per radial mode is defined as (Kjeldsen et al. 2008):

$$A = \frac{\sqrt{\frac{H_{\text{env}}\Delta\nu}{c}}}{\text{sinc}\left(\frac{\pi}{2}\frac{\nu_{\max}}{\nu_{\text{nyq}}}\right)}, \quad (1)$$

where H_{env} is the height of the power excess hump, and c is the effective number of modes per order, adopted as 3.04 (Bedding et al. 2010; Stello et al. 2011). We note that this value should in principle be adjusted for dipole-mode suppressed stars (Stello et al. 2016), but this is beyond the scope of this paper. The attenuation of oscillation amplitude due to the integration of photons every long-cadence interval (29.4 min) has been corrected with a sinc function (Huber et al. 2010; Murphy 2012; Chaplin et al. 2014a). Granulation power has also been corrected for this reason.

We used the SYD pipeline for extracting the granulation and seismic parameters mentioned above (Huber et al. 2009). The literature ν_{\max} values were assigned as initial guesses in the pipeline to model the power spectrum background. To obtain uncertainties for each parameter, we perturbed the power density spectrum 200 times with a χ^2 distribution with two degrees of freedom, repeated the fitting procedures on each perturbed spectrum, and calculated the standard deviation of the resulting output parameter distributions as the formal uncertainties (Huber et al. 2011a). Results returned from the pipeline were verified by visual inspection for over 17,700 individual targets to remove a fraction (9.1%) of wrong detections (non-oscillators) or marginal detections mainly due to low signal-to-noise ratio, resulting in a sample of 16,094 oscillating red giants.

3. DETERMINATION OF SEISMIC STELLAR FUNDAMENTAL PROPERTIES

3.1. Comparison of ν_{\max} Measurements

Figure 3 shows a comparison of our ν_{\max} values to the six literature samples for 16,094 stars. Except for a few outliers, for which we have checked and confirmed our estimates by eye, our results show good agreement with the literature, displaying a median fractional residual of 0.2% and a scatter of 3.5%. We note that the ν_{\max} estimates are not measured with totally independent methods. Huber et al. (2011a), Stello et al. (2013), Huber et al. (2014) and Yu et al. (2016) all used versions of the

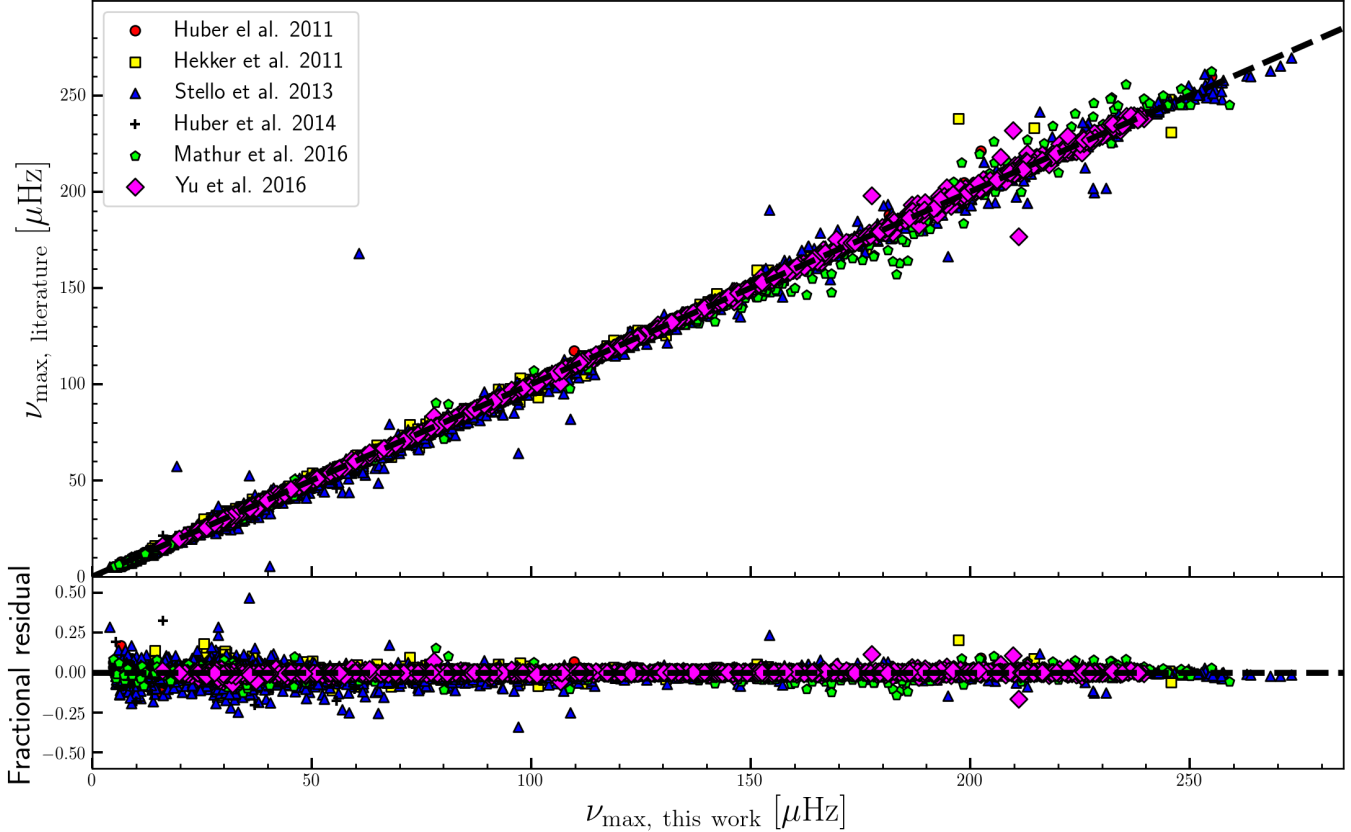


Figure 3. ν_{\max} comparison between our measurements and those from literature as shown in the legend. The black dash lines show the one-to-one relation in the top panel, and fractional residual in the bottom panel in the sense of $(\nu_{\max,\text{literature}} - \nu_{\max,\text{this work}}) / \nu_{\max,\text{this work}}$.

SYD pipeline (main difference in measuring $\Delta\nu$, see detail in Sec. 3.2), which is different from those employed by Hekker et al. (2011a) and Mathur et al. (2016). The comparison of ν_{\max} estimates from our work with those from Mathur et al. (2016) for 606 common stars shows a median fractional residual of -0.7% and a scatter of 4.5% . The comparison with the Hekker et al. (2011a) for 10,727 common starsshow a median fractional residual of -0.8% and a scatter of 10.7% . The larger scatter between our results and Hekker et al. (2011a) is mainly due to the fact that Hekker et al. (2011a) used only Q1 time series, resulting in some incorrectly measured ν_{\max} values, presumably due to low signal-to-noise ratio spectra.

From the bottom panel we notice that a significant spread occurs in the ν_{\max} range corresponding to red clump stars, roughly around $30 \mu\text{Hz}$, and to high-luminosity red giants less than approximately $10 \mu\text{Hz}$. We found the fractional residuals rise with decreasing ν_{\max} . The significant spread at $\nu_{\max} \approx 30 \mu\text{Hz}$ is an apparent effect due to a larger number of stars in this parameter range, which is also present in the ν_{\max}

comparison performed by Hekker et al. (2011b). The significant spread among stars with ν_{\max} less than $10 \mu\text{Hz}$ is associated with larger measurement uncertainties due to the higher frequency resolution required for these stars. Those high-luminosity red giants were generally observed with 25% fewer data points than stars with $\nu_{\max} \sim 200 \mu\text{Hz}$, as a result of *Kepler* target selection effects (Batalha et al. 2010). The second reason is related to the fewer detectable modes for measuring ν_{\max} . These stars have only approximately three orders of detectable modes (Stello et al. 2014), which due to the stochastic nature of the mode excitation can result in large uncertainties in ν_{\max} measurements. Another spread arises from the Mathur et al. (2016) sample, as shown with green filled pentagons. This presumably arises from the fact that those stars are distant low-luminosity red giants. The use of different methods to measure global oscillation parameters also contributes to the scatter. For further details on the comparison of different methods for determination of global seismic parameters, we refer the reader to Hekker et al. (2011b); Verner et al. (2011), and Hekker et al. (2012).

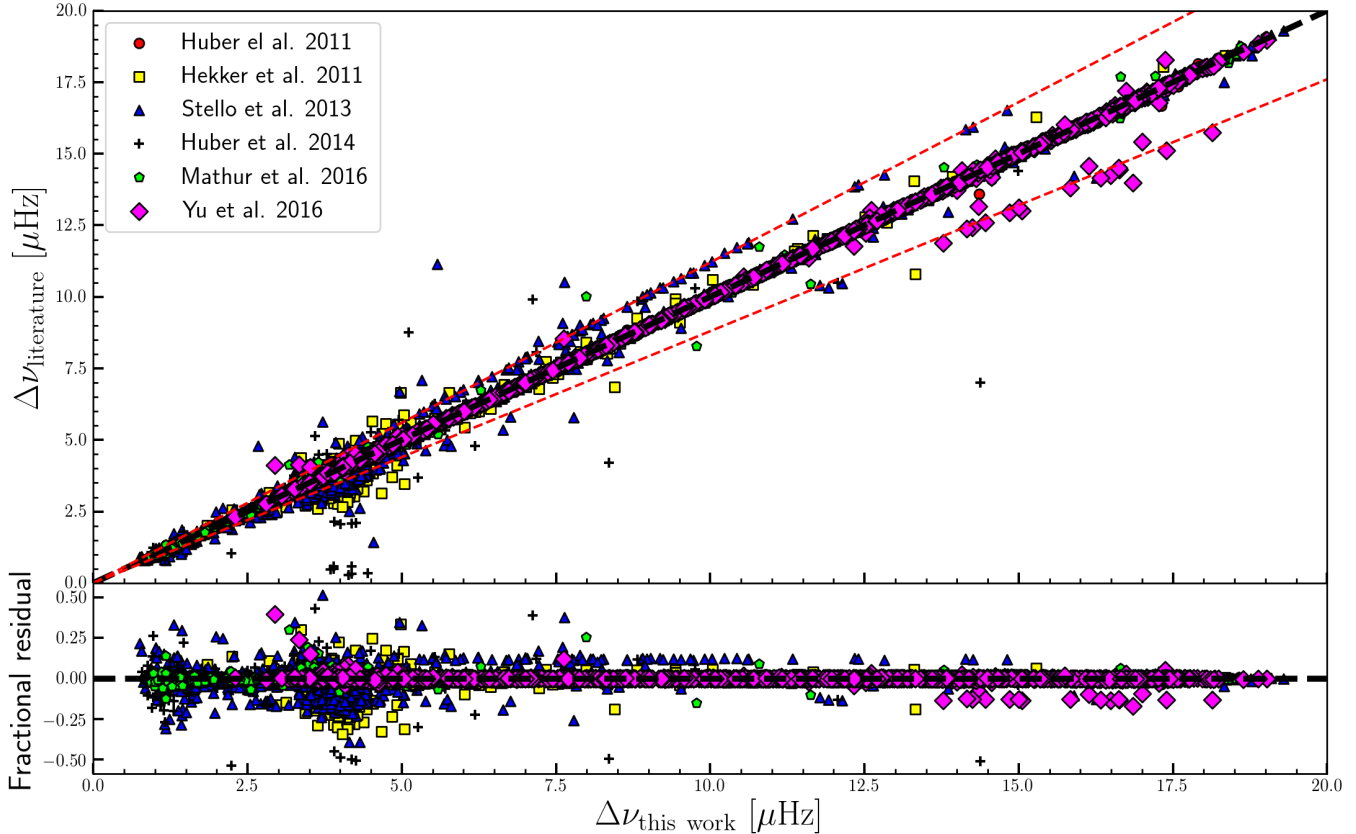


Figure 4. Same as figure 3 but for $\Delta\nu$, except here we added two additional red dashed lines representing a 12% deviation from the one-to-one relation, roughly equivalent to $\Delta\nu \pm \delta\nu_{02}$ (see text).

3.2. Comparison of $\Delta\nu$ Measurements

Figure 4 shows the comparison of $\Delta\nu$ measurements from different methods for 16,094 stars. The fractional residuals show two groups of stars, with the first one lying around $\Delta\nu \simeq 1.3 \mu\text{Hz}$ and the second one between approximately $3.3 \mu\text{Hz}$ and $5 \mu\text{Hz}$. The first group associated with high-luminosity red giants is related to low frequency resolution and to having few orders of detectable oscillation frequencies. The second group mainly corresponds to red clump stars, which have less regular and less clean power spectra. A combination of broad linewidths, mixed modes, rotational splittings and acoustic glitches can lead to large autocorrelations in a broad frequency range around the real $\Delta\nu$ values. Those effects were also present in the comparison work presented by Hekker et al. (2011b). Overall, our results are consistent with the literature, with a median fraction residual of 0.01% and a scatter of 4.2%. The comparison of our $\Delta\nu$ estimates with the different method of Mathur et al. (2016) or 606 common stars shows an absolute median fractional residual of $<0.01\%$ and a scatter of 3.8%. The comparison with Hekker et al. (2011a) for

10,727 common stars shows a median fraction residual of 0.8% and a scatter of 14.4%.

There are a number of stars (blue triangles) from the Stello et al. (2013) sample with measured $\Delta\nu$ values systematically 12% larger than our measurements (red dash line above the one-to-one relation). Those $\Delta\nu$ values correspond to the frequency differences $\delta\nu = \nu_{n+1,l=0} - \nu_{n-1,l=2} = \Delta\nu + \delta\nu_{02}$. This is confirmed by comparing the measurements of the small frequency separation $\delta\nu_{02}$, which roughly has a fixed ratio $\delta\nu_{02}/\Delta\nu = 0.121$, as measured by Huber et al. (2010). There are also some stars from the Stello et al. (2013) and Yu et al. (2016) samples, with $\Delta\nu$ values systematically 12% smaller than the ones determined in this work (red dash line below the one-to-one relation). Those values are the frequency differences $\delta\nu = \nu_{n,l=2} - \nu_{n,l=0} = \Delta\nu - \delta\nu_{02}$. These incorrect $\Delta\nu$ measurements from the literature also contribute to the scatter seen for the two groups of stars.

To understand the errors in $\Delta\nu$ measurements in Stello et al. (2013) and Yu et al. (2016), we note that, in the original SYD pipeline, the resulting $\Delta\nu$ value was determined to be whichever of the 10 highest peaks of

the autocorrelation function is closest to the predicted $\Delta\nu$. This suggests that a less accurately *predicted* $\Delta\nu$, based on the ν_{\max} - $\Delta\nu$ power-law relation, could lead to an incorrectly *measured* $\Delta\nu$ value, such as, $\Delta\nu - \delta\nu_{02}$ or $\Delta\nu + \delta\nu_{02}$. Given that the real $\Delta\nu$ value generally corresponds to a larger autocorrelation compared to $\Delta\nu - \delta\nu_{02}$ and $\Delta\nu + \delta\nu_{02}$, we weighted the autocorrelation functions using a Gaussian function centered at the predicted $\Delta\nu$ with a width of 30% or 70% of the predicted $\Delta\nu$. The higher width (70%) was specifically assigned to stars with ν_{\max} in the range $15 \mu\text{Hz} < \nu_{\max} < 60 \mu\text{Hz}$, which is mostly occupied by red clump stars. The lower width (30%) was applied to stars with ν_{\max} outside this range, and its reliability was confirmed by noting that $\Delta\nu$ values of RGB and secondary clump stars are much less sensitive to the selected width. The highest weighted peak was adopted as the resulting $\Delta\nu$ value. We found this method works well to correct those 12%-biased measurements. All measured global oscillation parameters were visually verified and are listed in Table 1.

3.3. Asteroseismic Scaling Relations

Brown et al. (1991) suggested that ν_{\max} would scale with the acoustic cutoff frequency and hence be related to stellar fundamental properties, as given by Kjeldsen & Bedding (1995) as follows:

$$\frac{\nu_{\max}}{\nu_{\max,\odot}} \simeq \left(\frac{M}{M_{\odot}} \right) \left(\frac{R}{R_{\odot}} \right)^{-2} \left(\frac{T_{\text{eff}}}{T_{\text{eff},\odot}} \right)^{-1/2}. \quad (2)$$

Here, $\nu_{\max,\odot} = 3090 \pm 30 \mu\text{Hz}$, $T_{\text{eff},\odot} = 5777\text{K}$. The other widely used scaling relation is related to the large frequency separation, $\Delta\nu$, which probes the sound speed profile and is proportional to the square root of the mean stellar density, as proposed by Ulrich (1986) as follows:

$$\frac{\Delta\nu}{\Delta\nu_{\odot}} \simeq \left(\frac{M}{M_{\odot}} \right)^{1/2} \left(\frac{R}{R_{\odot}} \right)^{-3/2}, \quad (3)$$

where $\Delta\nu_{\odot} = 135.1 \pm 0.1 \mu\text{Hz}$. The solar seismic reference values are obtained by analyzing the data collected by *SOHO/VIRGO* (Fröhlich et al. 1997) in the same way as the *Kepler* data analyzed (Huber et al. 2011b). By rearranging the scaling relations, stellar mass, M , radius, R , and surface gravity, g , can be readily derived as follows:

$$\frac{M}{M_{\odot}} \simeq \left(\frac{\nu_{\max}}{f_{\nu_{\max}} \nu_{\max,\odot}} \right)^3 \left(\frac{\Delta\nu}{f_{\Delta\nu} \Delta\nu_{\odot}} \right)^{-4} \left(\frac{T_{\text{eff}}}{T_{\text{eff},\odot}} \right)^{3/2}, \quad (4)$$

$$\frac{R}{R_{\odot}} \simeq \left(\frac{\nu_{\max}}{f_{\nu_{\max}} \nu_{\max,\odot}} \right) \left(\frac{\Delta\nu}{f_{\Delta\nu} \Delta\nu_{\odot}} \right)^{-2} \left(\frac{T_{\text{eff}}}{T_{\text{eff},\odot}} \right)^{1/2}, \quad (5)$$

$$\frac{g}{g_{\odot}} \simeq \frac{\nu_{\max}}{f_{\nu_{\max}} \nu_{\max,\odot}} \left(\frac{T_{\text{eff}}}{T_{\text{eff},\odot}} \right)^{1/2}. \quad (6)$$

Here $f_{\nu_{\max}}$ and $f_{\Delta\nu}$ are the potential correction factors for the ν_{\max} and $\Delta\nu$ scaling relations, respectively.

The stellar radius inferred from scaling relations has been tested to hold within $\sim 5\%$ for both dwarfs and giants using parallaxes, eclipsing binaries, cluster stars, and optical interferometry (Silva Aguirre et al. 2012; Brogaard et al. 2012; Huber et al. 2012; White et al. 2013; Huber et al. 2017). The stellar mass from the direct method has been tested to have $\sim 10\text{-}15\%$ uncertainties (Miglio 2012; Gaulme et al. 2016).

Some efforts have been made to mitigate possible systematics of the scaling relations. Miglio et al. (2012) proposed that a 2.7% (1.9%) correction factor of $\Delta\nu$ for red giants in NGC 6791 (NGC 6819) is necessary to minimize the difference in radius evaluated from the scaling relation and independent measurements of luminosity and effective temperature. Mosser et al. (2013a) pointed out that the observed large frequency separation, $\Delta\nu_{\text{obs}}$, measured at radial orders that were not high enough, is not equivalent to its asymptotic approximation, $\Delta\nu_{\text{as}}$, linked to the mean density of the star. A second-order term, for describing curvatures in the échelle diagram used for characterizing solar-like oscillations, was accounted for to revise the $\Delta\nu$ scaling relation. Hekker et al. (2013a), however, stated that the correction to the scaling relations is overestimated, by comparing $\Delta\nu_{\text{obs}}$ and $\Delta\nu_{\text{as}}$ from stellar models. Yıldız et al. (2016) argued that the $\Delta\nu$ scaling relation also depends on the adiabatic exponent at the surface, Γ_{1s} , but the application of their correction method is restricted to main-sequence stars. White et al. (2011); Guggenberger et al. (2016), and Guggenberger et al. (2017) proposed corrections to the $\Delta\nu$ scaling relations based on stellar models, including a dependence on temperature, metallicity, and mass. However, these corrections do not include He-core burning red giants, which make up roughly half of our sample. A similar approach suggested by Sharma et al. (2016) is to use a $\Delta\nu$ correction factor, $f_{\Delta\nu}$, which is a function of metallicity, T_{eff} , $\log g$, and evolutionary phase. The correction factor is obtained by interpolation in grids of models for $-3 < [\text{Fe}/\text{H}] < 0.4$ and $0.8 < M/M_{\odot} < 4.0$. We used this method to calibrate the $\Delta\nu$ scaling relation. The ν_{\max} calibration is more difficult since it cannot be calculated theoretically so far (Belkacem et al. 2011). Thus we set $f_{\nu_{\max}} = 1.0$ in this work.

3.4. Determination of Stellar Parameters

We combine ν_{\max} and $\Delta\nu$ from this work with effective temperatures from Mathur et al. (2017) to compile a

Table 1. Stellar Global Oscillation Parameters

KIC	Kp (mag)	Length (quarters)	Length (days)	ν_{\max} (μ Hz)	$\Delta\nu$ (μ Hz)	A (ppm)	Width (μ Hz)	Gran ($\text{ppm}^2/\mu\text{Hz}$)
2570518	14.72	17	1308.6	46.12(0.75)	4.934(0.012)	98.5(5.4)	16.7(1.3)	1312.6(335.8)
4682420	13.12	16	1221.3	128.72(1.27)	10.350(0.014)	32.8(1.8)	44.7(10.2)	63.8(10.6)
4946632	13.43	18	1318.2	199.32(1.08)	15.082(0.074)	45.8(3.5)	47.8(4.5)	25.8(12.5)
5340720	12.84	14	1023.4	94.88(0.71)	8.901(0.019)	57.7(2.9)	26.6(1.6)	311.9(76.8)
5446355	12.79	18	1317.8	8.04(0.25)	1.266(0.029)	277.3(22.2)	3.4(0.5)	92604.4(6767.2)
6197448	11.83	15	1138.8	50.45(1.18)	4.927(0.018)	58.1(2.8)	21.4(1.7)	1093.5(61.1)
6429836	13.83	5	371.3	38.82(0.53)	4.298(0.025)	120.1(6.4)	13.8(1.9)	2132.0(283.5)
6435899	13.53	6	380.7	21.50(0.42)	3.009(0.104)	180.5(9.0)	7.6(1.0)	9218.7(1309.2)
6756156	13.75	13	1013.9	160.46(1.10)	13.673(0.023)	43.7(2.3)	43.4(2.7)	75.5(22.0)
7445517	12.93	17	1308.5	64.39(0.80)	5.905(0.014)	58.9(2.9)	21.5(1.4)	654.9(84.6)
8265154	13.76	17	1308.9	208.08(1.79)	16.589(0.050)	–	–	–
8509198	13.80	10	777.2	108.95(1.29)	9.025(0.017)	33.3(2.1)	35.3(3.1)	145.8(32.4)
9285761	12.41	16	1221.0	53.23(0.47)	5.478(0.017)	84.7(4.5)	17.5(1.1)	1115.6(48.7)
9475300	12.75	18	1318.0	64.61(0.48)	6.303(0.011)	73.6(2.8)	20.6(1.1)	791.8(48.0)
10318430	12.03	18	1318.0	154.84(0.91)	12.985(0.032)	39.0(1.3)	45.9(2.3)	46.3(8.0)
10420502	12.78	7	467.3	32.28(0.65)	4.028(0.052)	135.2(5.7)	13.6(1.9)	4911.1(444.2)
10675935	12.95	15	1055.4	49.55(1.20)	4.897(0.069)	61.1(2.4)	21.6(1.8)	1008.4(49.9)
11026843	11.10	17	1235.3	30.27(0.63)	3.868(0.021)	132.1(5.4)	12.4(1.4)	5139.3(322.1)
11600442	8.85	15	1044.7	69.64(0.87)	6.048(0.044)	43.4(1.7)	24.8(1.5)	439.2(35.3)
12555883	12.57	14	1052.8	54.36(0.82)	5.242(0.014)	71.4(3.1)	21.0(1.6)	1200.1(75.5)

Notes: The length of dataset, in number of quarters (third column) and in days (fourth column), includes the 10-day commissioning run (Q0). The oscillation amplitude per radial mode, power excess width, and granulation power at ν_{\max} can be found in last three columns, for the stars with $\nu_{\max} \leq 200 \mu\text{Hz}$. The values in the brackets represent absolute formal uncertainties. (This table is available in its entirety in a machine-readable form in the online journal. A portion is shown here for guidance regarding its form and content.)

homogeneous catalog of seismically-derived stellar mass, radius, and therefore surface gravity. We adopted the model-based method proposed by [Sharma et al. \(2016\)](#) to correct $\Delta\nu$ and applied the direct method for deriving mass, radius, and $\log g$. Since the correction factor $f_{\Delta\nu}$ is different for RGB and HeB stars, the classification of evolutionary stage is required. For this we used the results from [Bedding et al. \(2011\)](#), [Stello et al. \(2013\)](#), [Mosser et al. \(2014\)](#), [Vrard et al. \(2016\)](#), [Elsworth et al. \(2017\)](#), and [Hon et al. \(2017\)](#).

We provide three solutions of mass and radius estimates in Table 2, one with $\Delta\nu$ corrected assuming all the targets are RGB stars, one with $\Delta\nu$ corrected but assuming all the targets are HeB stars, and the third one without any $\Delta\nu$ correction. We recommend to use mass and radius estimates with the $\Delta\nu$ correction taken into account. Mass and radius values can be readily obtained from Table 2 if the evolutionary stage is known. The recommended evolution phases are given in the last column of Table 2. Given the length of time series and the oscillation signal-to-noise ratio for the tar-

gets in those samples, we gave the highest reliability to [Hon et al. \(2017\)](#) (which includes [Mosser et al. \(2014\)](#) and [Vrard et al. \(2016\)](#) as training samples), followed by [Elsworth et al. \(2017\)](#), [Bedding et al. \(2011\)](#), and [Stello et al. \(2013\)](#). Note that there are 713 stars without classifications, among which we label the 7 targets with $\nu_{\max} > 125 \mu\text{Hz}$ as RGB stars, and the remaining 706 star as unclassified. For convenience, we provide all three solutions for every star. Some users may prefer to apply different corrections, and also the evolutionary stages of some stars may be revised in future.

As shown in Figure 5, the $\Delta\nu$ correction leads to overall lower mass estimates. Radii are less affected since the radius scaling relation has less dependence on $\Delta\nu$ (Equation 5).

We can see from the mass histogram that our full sample covers a large stellar mass range, centered around $1.3 M_{\odot}$ and slightly skewed towards high-mass stars. The radius distribution sheds some light on the evolutionary stage. Red clump stars are expected to pile up around $11 R_{\odot}$ due to their slower evolutionary rates compared to

Table 2. Stellar Fundamental Properties

KIC	T_{eff} (K)	$\log g$ (c.g.s.)	[Fe/H]	No $\Delta\nu$ correction		$\Delta\nu$ corrected, RGB		$\Delta\nu$ corrected, Clump		Phase
				M (M_{\odot})	R (R_{\odot})	M (M_{\odot})	R (R_{\odot})	M (M_{\odot})	R (R_{\odot})	
2570518	4531(80)	2.383(0.011)	0.360(0.150)	1.70(0.13)	13.91(0.36)	1.55(0.13)	13.26(0.36)	1.72(0.13)	13.97(0.36)	1
4682420	4827(80)	2.161(0.023)	0.230(0.150)	1.42(0.29)	16.37(1.36)	1.36(0.29)	16.02(1.36)	1.43(0.29)	16.47(1.37)	1
4946632	4773(80)	1.769(0.021)	0.390(0.150)	1.15(0.20)	23.15(1.59)	0.99(0.20)	21.49(1.59)	1.12(0.20)	22.86(1.57)	1
5340720	4995(146)	2.394(0.010)	-0.298(0.300)	1.00(0.14)	10.51(0.67)	1.04(0.14)	10.74(0.67)	1.00(0.14)	10.52(0.67)	1
5446355	4336(80)	2.522(0.007)	-0.070(0.150)	1.72(0.08)	11.90(0.20)	1.54(0.08)	11.29(0.20)	1.72(0.08)	11.92(0.20)	1
6197448	4756(80)	1.668(0.011)	0.330(0.150)	0.86(0.08)	22.43(0.89)	0.71(0.08)	20.46(0.89)	0.84(0.08)	22.28(0.89)	2
6429836	4758(141)	2.534(0.012)	0.065(0.300)	1.71(0.17)	11.69(0.45)	1.67(0.17)	11.55(0.45)	1.75(0.17)	11.83(0.46)	1
6435899	4832(100)	2.471(0.011)	-0.410(0.300)	1.65(0.16)	12.37(0.50)	1.50(0.16)	11.80(0.50)	1.67(0.16)	12.43(0.50)	2
6756156	5070(151)	2.121(0.020)	-0.526(0.300)	2.71(0.41)	23.71(1.31)	2.60(0.41)	23.22(1.31)	2.73(0.41)	23.78(1.31)	1
7445517	4756(80)	2.899(0.007)	0.170(0.150)	1.32(0.07)	6.77(0.12)	1.30(0.07)	6.70(0.12)	1.36(0.07)	6.85(0.12)	1
8265154	4967(149)	2.458(0.009)	-0.414(0.300)	1.55(0.16)	12.15(0.54)	1.53(0.16)	12.08(0.54)	1.58(0.16)	12.27(0.55)	1
8509198	4993(162)	1.699(0.013)	-0.122(0.300)	1.15(0.12)	25.09(1.03)	0.99(0.12)	23.27(1.03)	1.11(0.12)	24.66(1.01)	1
9285761	4803(80)	2.772(0.005)	-0.170(0.150)	1.45(0.06)	8.19(0.11)	1.34(0.06)	7.89(0.11)	1.46(0.06)	8.23(0.11)	1
9475300	4783(80)	3.116(0.007)	-0.080(0.150)	1.42(0.07)	5.45(0.09)	1.39(0.07)	5.41(0.09)	1.44(0.07)	5.50(0.09)	1
10318430	5329(151)	2.940(0.008)	-0.307(0.300)	1.33(0.08)	6.47(0.13)	1.38(0.08)	6.58(0.13)	1.35(0.08)	6.53(0.13)	1
10420502	4735(80)	2.296(0.017)	0.030(0.150)	0.98(0.29)	11.66(1.62)	0.82(0.29)	10.66(1.62)	0.95(0.27)	11.47(1.58)	2
10675935	5129(154)	2.297(0.012)	-0.323(0.300)	0.83(0.08)	10.72(0.41)	0.74(0.08)	10.14(0.41)	0.83(0.08)	10.70(0.41)	2
11026843	5009(150)	2.466(0.019)	0.067(0.300)	1.40(0.20)	11.44(0.59)	1.31(0.20)	11.07(0.59)	1.41(0.20)	11.52(0.60)	2
11600442	5205(158)	2.441(0.007)	0.324(0.300)	1.19(0.07)	10.89(0.24)	1.11(0.07)	10.52(0.24)	1.20(0.07)	10.92(0.24)	2
12555883	4648(137)	1.921(0.013)	0.533(0.300)	1.21(0.13)	19.96(0.79)	1.04(0.13)	18.52(0.79)	1.18(0.12)	19.67(0.78)	1

Notes: T_{eff} and [Fe/H] are collected from Mathur et al. (2017), while surface gravity is seismically-derived from this work. Three solutions of stellar mass and radius are provided, corresponding to those with and without $\Delta\nu$ correction. Evolutionary phases are also given in the last column, 2 for HeB, 1 for RGB, and 0 for unclassified phase, with which stellar mass and radius can be obtained readily. For example, KIC 2570518 is an RGB star, whose mass and radius are respectively $1.55 \pm 0.13 M_{\odot}$ and $13.26 \pm 0.36 R_{\odot}$ after $\Delta\nu$ correction. The values in the brackets represent absolute uncertainties. (This table is available in its entirety in a machine-readable form in the online journal. A portion is shown here for guidance regarding its form and content.)

RGB stars. The sharp cutoff at the low-radius endpoint is associated with our sample selection, which does not include subgiants or main-sequence stars. As pointed out by Kallinger et al. (2010b), we expect to see a small excess near $R = 20.5 R_{\odot}$, made up of stars in the AGB clump phase (Cassisi et al. 2001). That excess is not readily apparent in our sample. Insets show close-ups of the distributions at high mass and radius. We checked the six most massive stars, with mass $> 4.5 M_{\odot}$, and found that they indeed show relatively smaller large separations than more typical stars at the same ν_{max} , resulting in larger seismically-inferred masses. The investigation of the underlying physics by means of individual frequency modeling is in preparation.

We also provide surface gravities for over 16,000 stars derived from the scaling relation (Equation 6). Surface gravity estimates from asteroseismic analysis are believed to be more precise ($\sim 2\%$, Hekker et al. 2013b), compared to the time scale technique ($\sim 4\%$, Kallinger

et al. 2016), the 8-hour “flicker” method ($\sim 25\%$, Bastien et al. 2013), spectroscopy ($\sim 50\%$, Valenti & Fischer 2005), and photometric colors ($\sim 100\%$, Brown et al. 2011). Seismically-derived $\log g$ values can be used as constraints to lift the degeneracy when spectroscopically deriving effective temperature, surface gravity, and metallicity (Bruntt et al. 2012; Huber et al. 2013b). Red clump stars are expected to lie at $\log g \sim 2.4$ dex. Figure 5 also indicates that our sample includes a significant number of low-luminosity red giants ($\log g \gtrsim 2.6$) and substantially fewer high-luminosity red giants ($\log g \lesssim 2.3$).

3.5. Uncertainties

The fractional uncertainties of seismic parameters and stellar fundamental properties are shown in Figure 6, based on full length end-of-mission long-cadence datasets. Considering output offset from different methods (Huber et al. 2017), we have added in quadrature

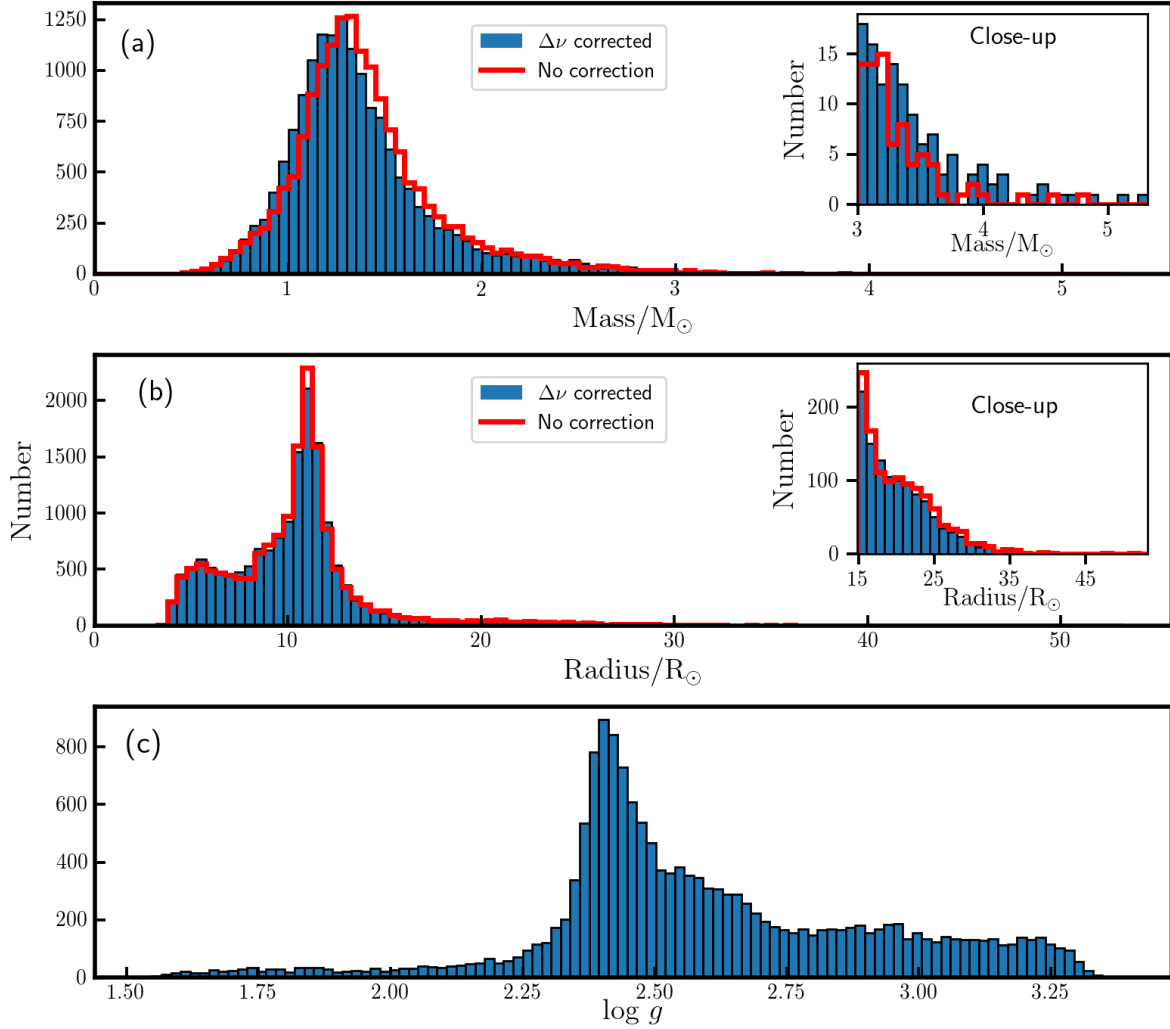


Figure 5. Histograms of seismically-inferred mass, radius and surface gravity. The distributions of (a) mass and (b) radius in blue have accounted for the $\Delta\nu$ correction using the scheme proposed by [Sharma et al. \(2016\)](#). For comparison, we also show the mass and radius distributions without the $\Delta\nu$ correction in red. The surface gravity distribution is plotted in panel (c). The insets show close-up of the distributions of high-mass and high-radius stars.

1.0% and 0.5% relative uncertainties in ν_{\max} and $\Delta\nu$ to their formal uncertainties, respectively, only when deriving the uncertainties for mass, radius, and $\log g$. The correction factor, $f_{\Delta\nu}$, was fixed when determining the uncertainties of mass and radius using error propagation.

It can be seen from Figure 6 that ν_{\max} and $\Delta\nu$ can be measured more precisely in RGB stars (blue) than in HeB stars (red). This is mainly because HeB stars generally exhibit more complicated power spectra. This effect is propagated into the estimates of mass, radius, and $\log g$, which are derived from the scaling relations.

The effective temperatures from [Mathur et al. \(2017\)](#) have four populations of distinct uncertainty distributions, from the KIC ([Brown et al. 2011](#), $\sim 4.0\%$),

the DR24 stellar properties catalog ([Huber et al. 2014](#), $\sim 4.0\%$), the revised catalog of temperatures for long-cadence stars in the KIC ([Pinsonneault et al. 2012](#), $\sim 3.0\%$), and the high-resolution spectroscopy from APOGEE DR12 ([Pinsonneault et al. 2014](#), $\sim 2.0\%$, and [Alam et al. 2015](#), $\sim 1.7\%$).

The uncertainty of the granulation power for RGB stars is bimodal with a significant peak at higher uncertainties, while the HeB has a similar distribution to the RGB at lower uncertainties. These features are a result of increasing fractional uncertainties of granulation power with ν_{\max} and combined with the star number distribution as function of ν_{\max} of the entire sample. For the subsample with $\nu_{\max} < 30 \mu\text{Hz}$, we found that RGB and HeB stars have very similar and single-peaked

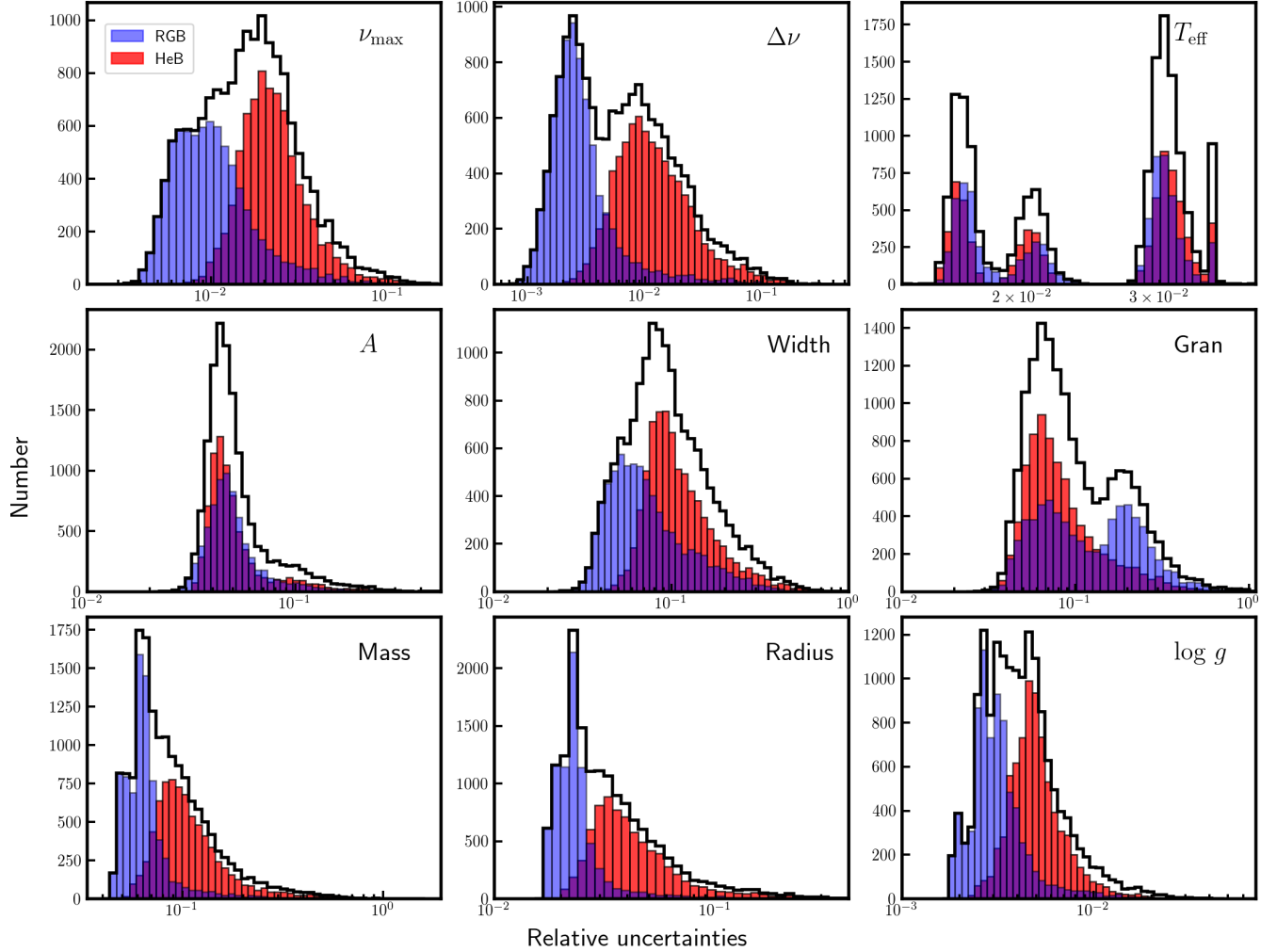


Figure 6. Relative uncertainty distributions of global oscillation parameters and stellar fundamental properties for 16,094 stars. When deriving the uncertainties of mass, radius, and $\log g$, we have added 0.5% and 1% uncertainties in quadrature to the formal uncertainties of $\Delta\nu$ and ν_{\max} , respectively. The blue and red bars show overlapping distributions of RGB and HeB stars, respectively, while the black histogram displays the sum of all the stars, including the 706 stars with unclassified (RGB or HeB) evolutionary phase.

fractional uncertainty distributions that peak just below 0.1. As ν_{\max} increases, we see the right component gradually more clearly.

As expected, longer datasets enable us to determine global seismic parameters more precisely (Hekker et al. 2012). Thanks to the full-mission data sets used in our asteroseismic analysis (see Fig. 1), we report precise determinations of global seismic parameters and stellar fundamental properties, with typical (median) precisions of 1.6% in ν_{\max} , 0.6% in $\Delta\nu$, 4.7% in oscillation amplitude, 8.6% in granulation power, 8.8% in width of power excess, 7.8% in mass, 2.5% in radius, and 0.01 dex (or 0.3%) in $\log g$. Considering only the 7839 stars with near full-mission data (time series longer than 1200 days), the uncertainty distributions shift slightly to

lower values, while the overall distributions shapes look similar. The typical (median) fractional uncertainties are 1.4% in ν_{\max} , 0.4% in $\Delta\nu$, 4.6% in oscillation amplitude, 7.8% in granulation power, 7.9% in width of power excess, 6.9% in mass, 2.5% in radius, and 0.01 dex (or 0.3%) in $\log g$. The seismic and non-seismic parameters and their uncertainties are given in Table 1 and 2.

3.6. Correlation between ν_{\max} and $\Delta\nu$

Figure 7 displays the well-established power-law relation between $\Delta\nu$ and ν_{\max} (Hekker et al. 2009; Stello et al. 2009; Huber et al. 2011a). The red dashed line shown in Figure 7a was fitted using an MCMC method and is expressed as $\Delta\nu = \alpha \cdot (\nu_{\max})^{\beta}$, where $\alpha = 0.267 \pm 0.002$, $\beta = 0.764 \pm 0.002$. As noted pre-

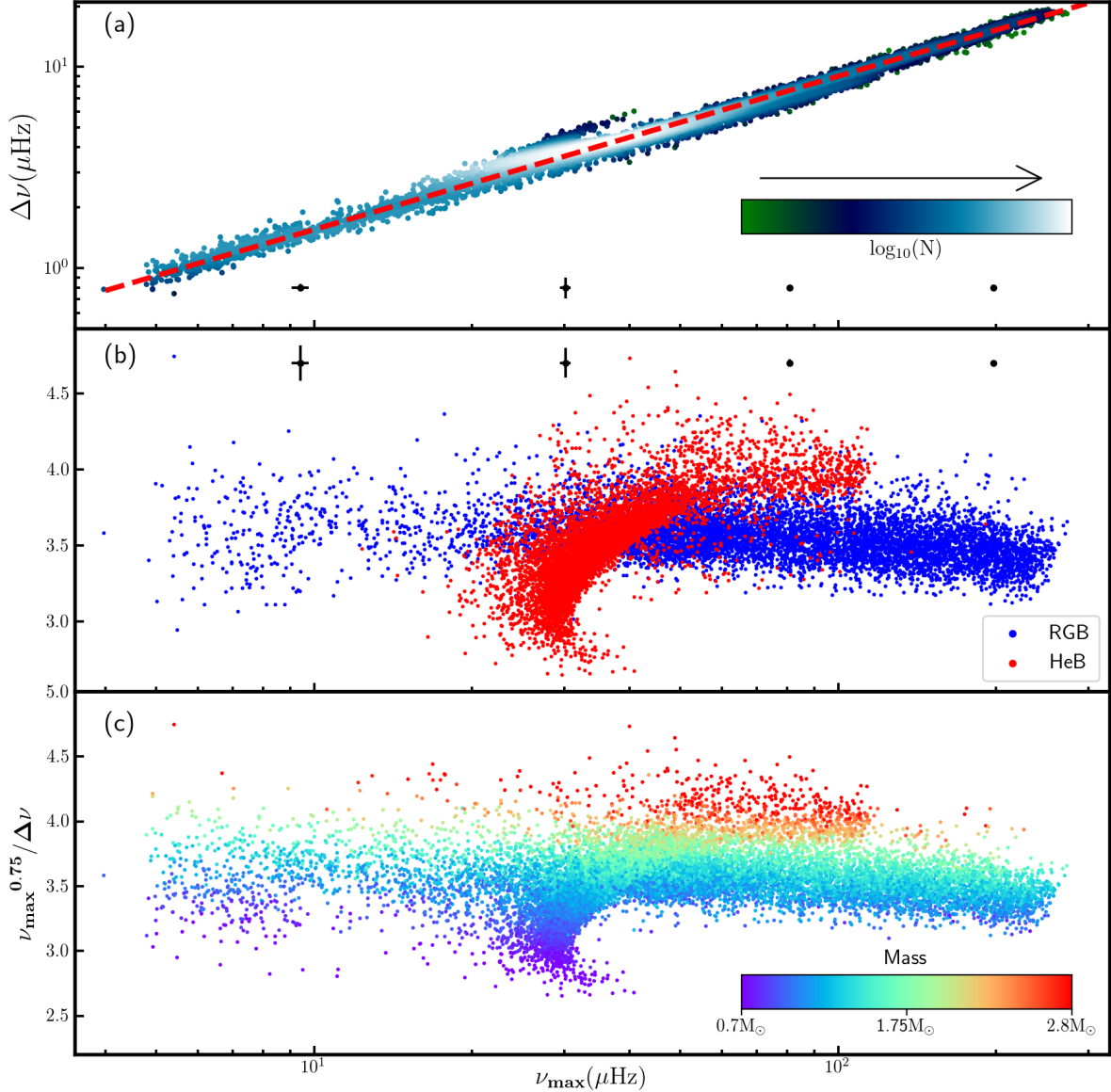


Figure 7. (a) Power-law relation between ν_{\max} and $\Delta\nu$ with number density of stars color-coded. The red dashed line is fitted using MCMC as $\Delta\nu = \alpha \cdot (\nu_{\max})^{\beta}$, where $\alpha = 0.267 \pm 0.002$, $\beta = 0.764 \pm 0.002$. (b) The scatter relative to the global trend color-coded with evolutionary phase. Stars without the phase classification, flagged as 0, are not shown here. Typical uncertainties are displayed. (c) Similar as panel (b) but color-coded with seismically-inferred mass (see Section 3.4).

viously in the literature, the power law is unable to perfectly describe the relation between ν_{\max} and $\Delta\nu$, especially in the common parameter space of RGB and HeB stars (Huber et al. 2011a). We can also see a concentration of HeB stars constituting a hook originating from around $\nu_{\max} \simeq 30 \mu\text{Hz}$, which we identify as the zero-age main sequence for helium-core burning.

In order to show this feature more clearly, we plotted $\nu_{\max}^{0.75}/\Delta\nu$ as a function of ν_{\max} in Figure 7b and 7c, color-coded by evolutionary phase and stellar mass,

respectively. The ordinate, $\nu_{\max}^{0.75}/\Delta\nu$, has mass dependence expressed as follows, by combining Equation 2 and 3:

$$\frac{(\nu_{\max}/\mu\text{Hz})^{0.75}}{\Delta\nu/\mu\text{Hz}} \simeq \left(\frac{M}{M_{\odot}} \right)^{0.25} \left(\frac{T_{\text{eff}}}{T_{\text{eff},\odot}} \right)^{-0.375}. \quad (7)$$

Since red giants cover a relatively small range of effective temperature, there is a very minor effective temperature influence on the distribution in Figure 7b and 7c. A pronounced feature in Figure 7b is the distinct distributions of HeB and RGB stars. The HeB stars form a sharp

hook-shaped structure originating from $\nu_{\max} \sim 30 \mu\text{Hz}$ (low-mass stars) and extending to ν_{\max} at $\sim 120 \mu\text{Hz}$ (high-mass stars). Note that there exists a sharp and extremely well-defined edge related to red clump stars. This is likely associated with the fact that all stars below roughly $2 M_{\odot}$ ignite helium in fully degenerate cores of very similar mass. This sharp edge also tells us that the scaling relations work well for the zero-age main sequence of HeB stars.

In Figure 7c we note that some red clump stars have low mass around or below $0.7 M_{\odot}$. The lack of low-luminosity RGB stars ($\nu_{\max} > \sim 40 \mu\text{Hz}$) with such low mass implies that there could be systematics in mass inferred with the scaling relations, or that at least some of those low mass RGB stars undergo mass loss before reaching the HeB phase. Assuming the latter is the case, the slightly less sharp edge toward the lowest mass HeB stars, at roughly $\nu_{\max}^{0.75}/\Delta\nu \simeq 2.8$ and $\nu_{\max} \simeq 30 \mu\text{Hz}$, could be a sign of “chaotic” variation in mass loss. In addition, the lack of low mass stars ($\lesssim 0.7 M_{\odot}$), marked by purple dots, at higher ν_{\max} regime ($\gtrsim 40 \mu\text{Hz}$) and the presence of the low mass stars in the range $\nu_{\max} \lesssim 20 \mu\text{Hz}$ possibly suggest that the low mass stars with $\nu_{\max} \lesssim 20 \mu\text{Hz}$ are in the AGB phase and have experienced mass loss.

3.7. Seismic H-R diagram

Figure 8 shows a seismic Hertzsprung-Russell (H-R) diagram for the largest sample of *Kepler* solar-like oscillators so far, with $\Delta\nu$ being measured from this work for red giants, except for super-Nyquist red giants from Yu et al. (2016), and from Huber et al. (2011a) for main-sequence and subgiant stars. We select $\Delta\nu$ rather than ν_{\max} to illustrate the seismic H-R diagram because $\Delta\nu$ can be more accurately measured for stars oscillating around the Nyquist frequency. Red giants oscillate with amplitudes ranging from a few tens to thousands of parts per million, as shown in the color. The characteristic oscillation timescales vary from hours up to days, as indicated by ν_{\max} plotted on the right. A few outliers are present, mainly due to the poorly-determined temperatures for those stars (Mathur et al. 2017). The large uncertainties of the temperatures blur the distributions of red clump stars, making it difficult to distinguish from RGB stars. We observe a sharp edge lying at $\nu_{\max} \simeq 275 \mu\text{Hz}$ ($\Delta\nu \simeq 19.2 \mu\text{Hz}$), corresponding to the upper limit of ν_{\max} estimates in this work. Solar-like oscillations with ν_{\max} greater than the long-cadence Nyquist frequency are generally detected with short-cadence data (Gilliland et al. 2010). Murphy et al. (2013) and Chaplin et al. (2014a), however, pointed out that it remains possible to detect these oscillation using

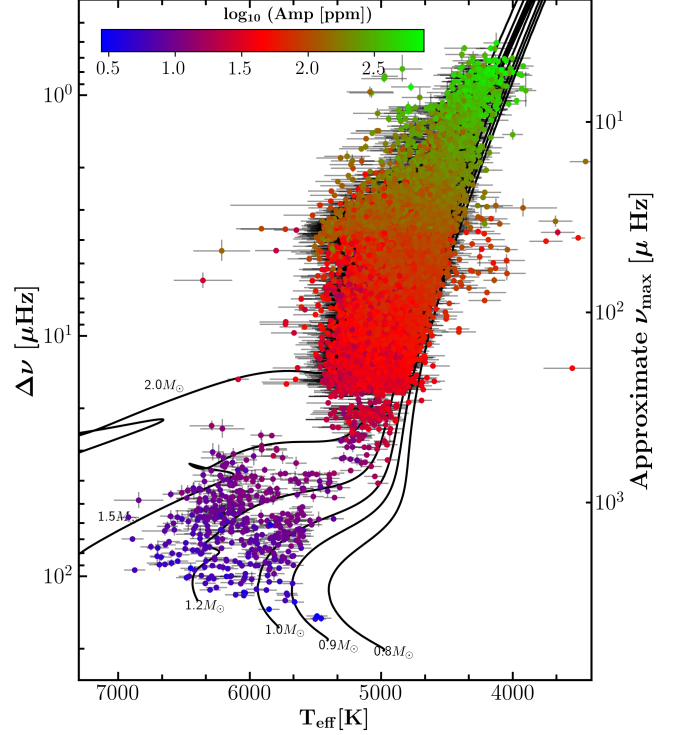


Figure 8. Seismic H-R diagram ($\Delta\nu$ vs T_{eff}). The estimates of $\Delta\nu$ are from this work for red giants, except for super-Nyquist red giants from Yu et al. (2016). The values of $\Delta\nu$ for main-sequence and subgiant stars are collected from Huber et al. (2011a). Approximate ν_{\max} values are shown to the right axis. Logarithmic oscillation amplitude per radial mode is color-coded. Solid lines show solar-metallicity evolutionary tracks with mass labeled. Temperatures are adopted from Mathur et al. (2017).

long-cadence data. Yu et al. (2016) subsequently identified 98 stars oscillating in the super-Nyquist frequency regime, up to 387 Hz. These super-Nyquist red giants are also plotted in Figure 8.

4. MASS AND METALLICITY EFFECTS ON POWER EXCESS PARAMETERS

4.1. Power excess difference in RGB and HeB stars

Figure 9 shows that RGB and HeB stars follow different distributions of oscillation amplitude, granulation power, and the width of power excess (see Section 3.4 for the evolutionary phase classification). The differences are negligible for low ν_{\max} red clump stars ($\nu_{\max} \simeq 30 \mu\text{Hz}$), but gradually become substantial for higher ν_{\max} stars ($\nu_{\max} \simeq 60 \mu\text{Hz}$), and significant for secondary clump stars (HeB stars that did not undergo a helium flash, due to the non-degenerate helium core). We confirm that secondary clump stars have lower oscillation amplitudes and granulation power, and broader

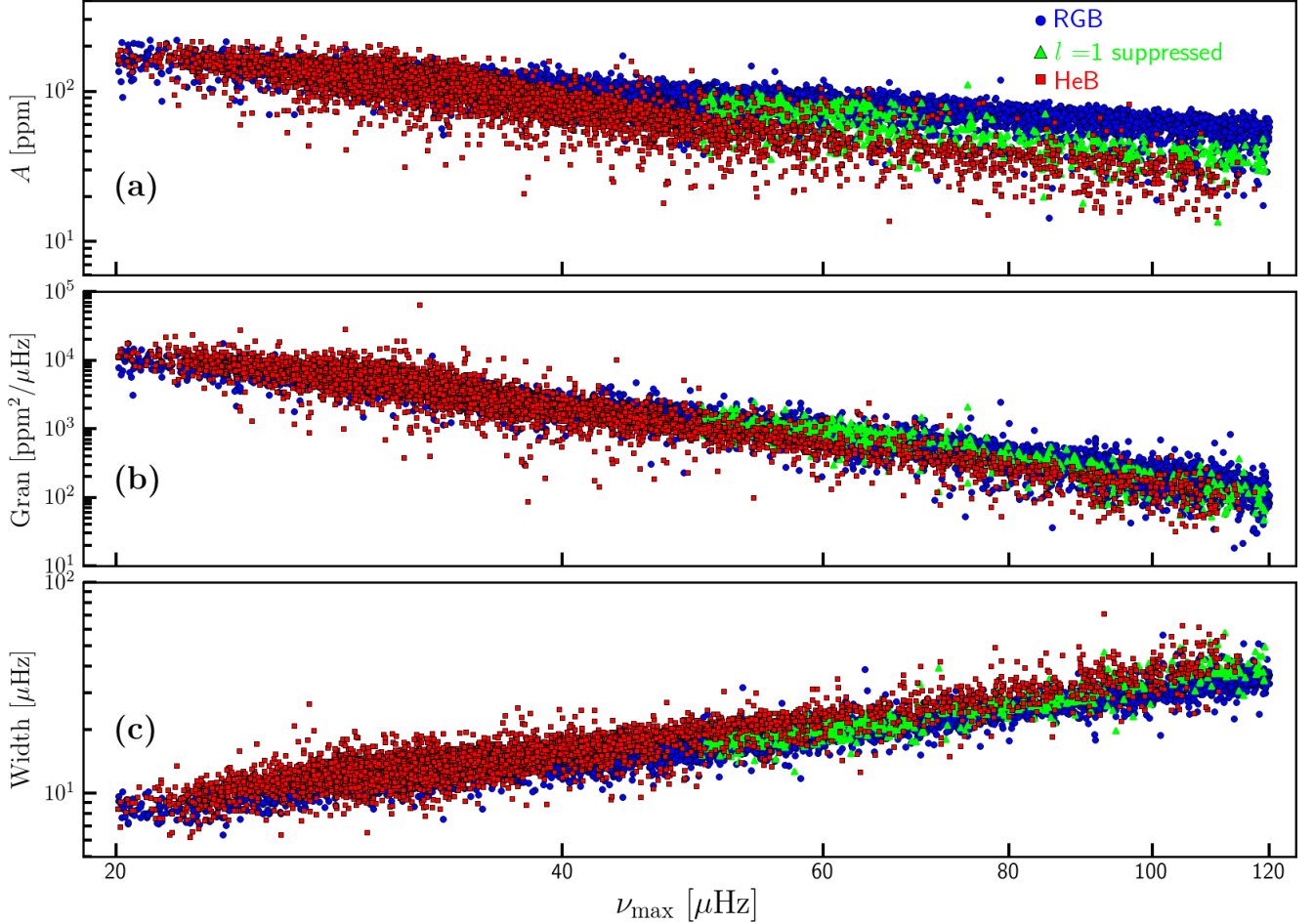


Figure 9. The distributions of (a) oscillation amplitude, (b) granulation power measured at ν_{\max} , and (c) width of power excess for RGB (blue circles) and HeB (red squares) stars. The green triangles show dipole-mode suppressed oscillators (Stello et al. 2016).

power excesses compared to RGB stars at a given ν_{\max} (Mosser et al. 2012a). We have tested and found that the offsets of both oscillation amplitude and granulation power between RGB and clump stars, in the range $50 \mu\text{Hz} < \nu_{\max} < 120 \mu\text{Hz}$, are mainly due to the difference in stellar mass between the two populations, followed by luminosity and temperature, using the formulas fitted by Huber et al. (2011a). The oscillation amplitude and granulation power show tight correlations, and both increase when the star evolves up the RGB (Kjeldsen & Bedding 2011; Huber et al. 2011a; Kallinger et al. 2014).

We checked whether the smoothing process is responsible for the broader power excesses of secondary clump stars. One might suspect that the broader power excess of a secondary clump star could artificially arise from the smoothing process applied to measure it. To test this, we selected 20 RGB and secondary clump stars, including stars having extreme width values, with the same

ν_{\max} values in the range $60 \mu\text{Hz} < \nu_{\max} < 120 \mu\text{Hz}$ and checked individual original power spectra without smoothing. We found the power excess of the secondary clump stars to be intrinsically broader than the RGB stars. Therefore, the difference of power excess width in Figure 9c is not a measurement bias. The broader power excess might reduce the precision when measuring ν_{\max} , which will propagate into the seismic determinations of mass and radius.

The measured amplitude of dipole-mode suppressed RGB stars (Stello et al. 2016), as shown in Figure 9a, is smaller than that of normal RGB stars. This is a simple consequence of the lack of power in the dipole modes, which constitute about half the total power (Stello et al. 2016). We find that the suppressed stars show $\sim 9\%$ less granulation power than normal RGB stars, as shown in Figure 9b. This offset is presumably caused by the mass difference between the dipole-mode suppressed stars and the normal RGB stars. To understand this, we recall

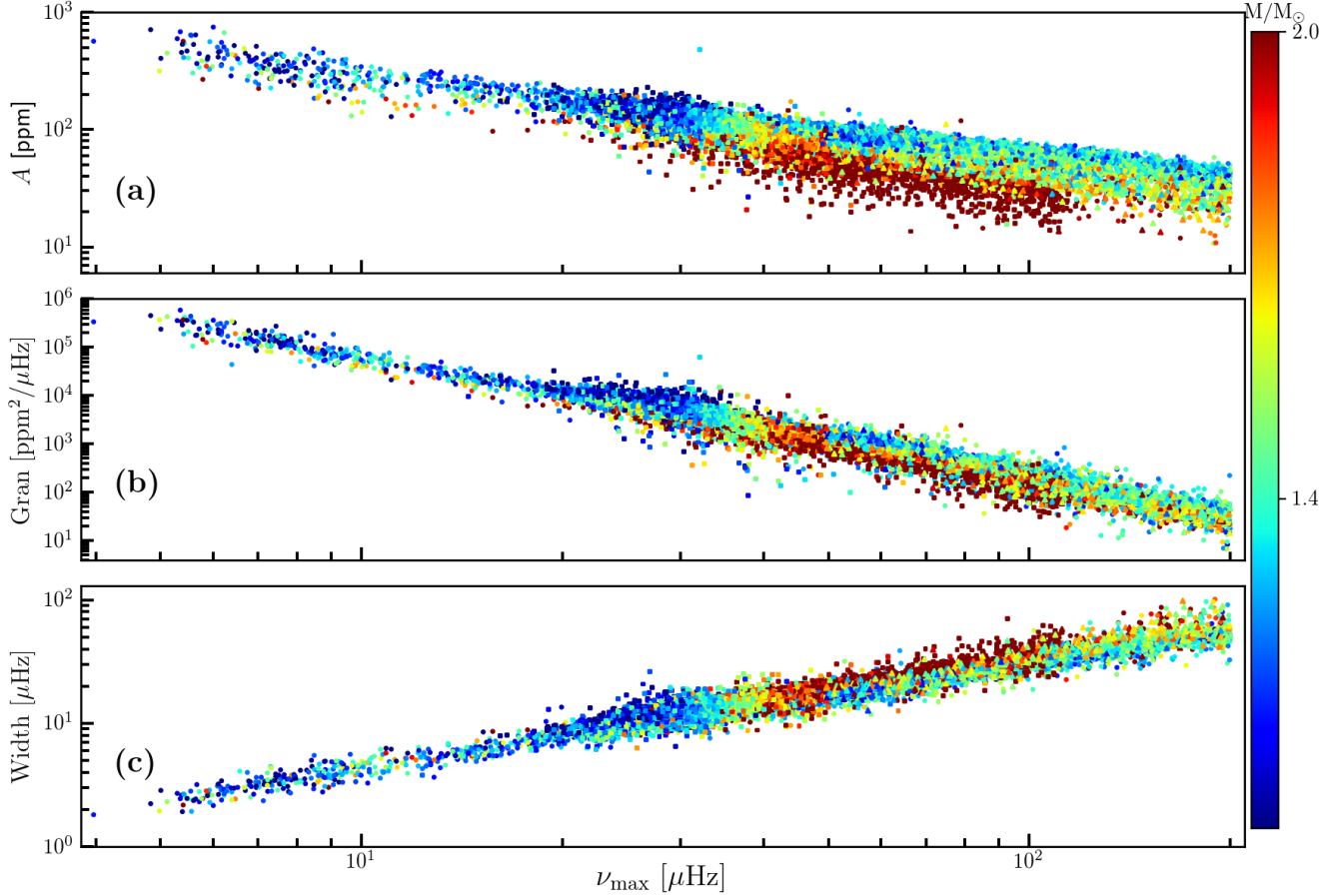


Figure 10. The distributions of (a) oscillation amplitude, (b) granulation power measured at ν_{\max} , and (c) width of power excess for all red giants, color-coded by seismic mass that is truncated to display the mass effect. The measurements at ν_{\max} greater than $200 \mu\text{Hz}$ are not shown because of the difficulty in modeling spectrum background when power excess approaches the Nyquist frequency. The Symbols have same meaning as in Figure 9

that (1) dipole-mode suppressed stars show a mass distribution shifted to larger masses compared to normal RGB stars (see Figure 10a, and Figure 2 in Stello et al. 2016). (2) Granulation power is a decreasing function of stellar mass, as predicted by Kjeldsen & Bedding (2011). (3) The granulation power of dipole-mode suppressed stars follows the same relations as normal red giants (García et al. 2014).

4.2. Mass effect

Many efforts have been made to investigate the dependence of oscillation amplitude and granulation power on stellar fundamental properties in field stars and open clusters (e.g., Kjeldsen et al. 2008; Kjeldsen & Bedding 2011; Stello et al. 2011; Huber et al. 2011a; Mathur et al. 2011; Mosser et al. 2012a; Corsaro et al. 2013; Kallinger et al. 2014; Corsaro et al. 2017). The empirical relations as proposed by Kjeldsen et al. (2008) and Kjeldsen & Bedding (2011) predict that oscillation amplitude and granulation power depend on the luminosity, mass, and

temperature. In this section we study the mass influence on oscillation and granulation using our sample of over 16000 oscillating red giants.

As shown in Figure 10a, the oscillation amplitude is a decreasing function of ν_{\max} , ranging from ~ 600 ppm at $\nu_{\max} \approx 5 \mu\text{Hz}$ down to ~ 20 ppm at $\nu_{\max} \approx 200 \mu\text{Hz}$. We observe an extremely sharp upper boundary, which might be related to excitation and damping of oscillation modes. We note that there are a number of stars with low amplitudes along the bottom of the global trend. We have checked those stars and found that some have low S/N power spectra, with *Kepler* time series that are only a few quarters long. The low-amplitude stars could also be contaminated by nearby stars or diluted by their companions in binary systems (Ziegler et al. 2017; Schonhut-Stasik et al. 2017) or be exotic stars. Figure 10a also shows that high-mass HeB stars have overall lower amplitudes compared to RGB stars at a given ν_{\max} . A clear mass gradient is present in RGB stars as well.

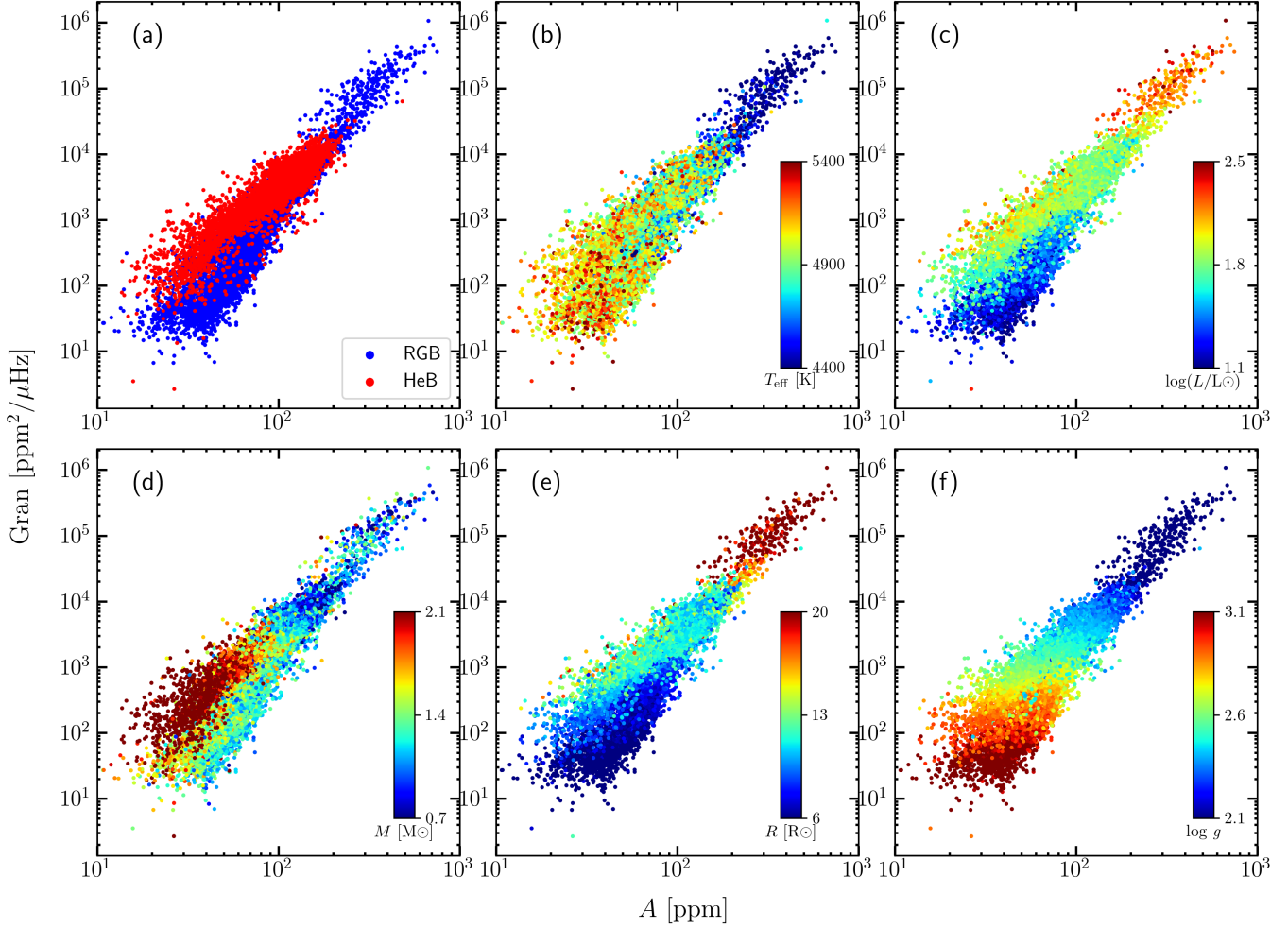


Figure 11. Relation of oscillation amplitude and granulation power, color-coded by (a) evolutionary phase, (b) effective temperature, (c) luminosity, (d) mass, (e) radius, and (f) $\log g$. Stars with $\nu_{\text{max}} > 200 \mu\text{Hz}$ are excluded.

The granulation power determined at ν_{max} has a dependence on stellar mass, as shown in Figure 10b. Our results are in qualitative agreement with the predictions given by Kjeldsen & Bedding (2011), where higher-mass stars are expected to have lower oscillation amplitude and granulation power (Mosser et al. 2012a).

Red giants show progressively narrower power excess when evolving towards the tip of the RGB. Only approximately three orders of modes can be detected in high-luminosity red giants with $\nu_{\text{max}} \simeq 5 \mu\text{Hz}$ and seven orders of modes in low-luminosity red giants (Stello et al. 2014; Corsaro et al. 2015). We confirm that the width of power excess is an increasing function of stellar mass as shown in Figure 10(c) (see also Mosser et al. 2012a). Higher mass stars with wider power excess and lower oscillation amplitude implies that the total oscillation power tends to be almost conserved among the stars of different mass (Kallinger et al. 2014).

As shown in Figure 10, granulation power correlates with oscillation amplitude. To see this more clearly, we plotted oscillation amplitude against granulation power in Figure 11a, color-coded by the evolutionary phase (RGB or HeB). The correlations are similar but distinct for RGB and HeB stars (Kallinger et al. 2014). The two populations following different distributions are mainly caused by their different stellar fundamental properties: luminosity, mass, and temperature (thus radius and $\log g$), as we can see from Figures 11b-f. The temperature effect stands out among RGB stars but is not clear between RGB and HeB at a given oscillation amplitude, because of their similar temperatures. Our results are qualitatively consistent with the predictions by Kjeldsen & Bedding (2011).

4.3. Metallicity effect

Figure 12 shows the ν_{max} -amplitude relation color-coded by metallicity. We observe that in Figure 12a the

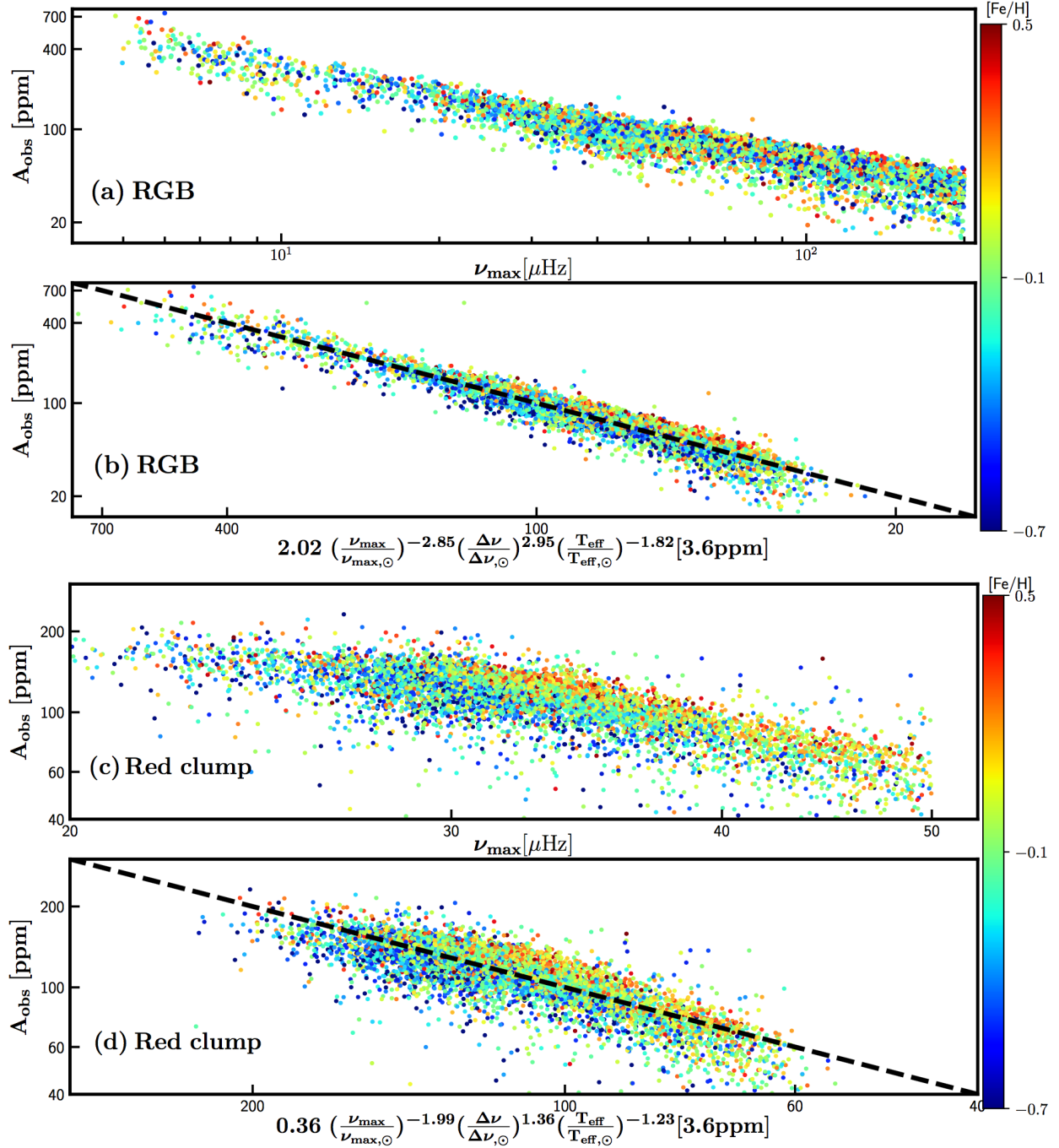


Figure 12. Metallicity influence on oscillation amplitude of RGB and red clump stars. (a) Observed oscillation amplitude is plotted against ν_{max} , color-coded by metallicity. (b) The observed oscillation amplitude is compared to its calculated counterpart using the model of equation 8. Panels c and d are similar to a and b but for red clump stars, separated from secondary clump stars with a threshold of $\nu_{\text{max}}=50 \mu\text{Hz}$. The black dash line shows the one-to-one relation. Stars with $\nu_{\text{max}} > 200 \mu\text{Hz}$ have been excluded due to the difficulty of modeling granulation background.

metallicity effect is not visually striking, which is due to the fact that oscillation amplitudes have stronger dependence on luminosity, mass, and temperature (Kjeldsen & Bedding 2011), blurring the possible metallicity influence. In this section we attempt to investigate the metallicity effect on oscillation and granulation. Instead of fitting to luminosity and mass inferred from the scaling relations with possible systematics, we fit the oscillation amplitude as a function of the observables, ν_{\max} , $\Delta\nu$, and temperature, as:

$$\frac{A}{A_{\odot}} = \alpha \left(\frac{\nu_{\max}}{\nu_{\max,\odot}} \right)^{\beta} \left(\frac{\Delta\nu}{\Delta\nu,\odot} \right)^{\gamma} \left(\frac{T_{\text{eff}}}{T_{\text{eff},\odot}} \right)^{\delta}. \quad (8)$$

Here α is a scaling factor introduced so that our model does not have to pass through the solar reference point ($A_{\odot} = 3.6$ ppm). Equation 8 was converted to a logarithmic scale when implementing the fit. We attempted to study the metallicity influence on RGB and HeB stars separately, because the two populations have different distributions as shown in Figure 9a and Figure 10a. In this work, metallicity estimates are adopted from Mathur et al. (2017). We excluded all the stars with $\nu_{\max} > 200 \mu\text{Hz}$ because the backgrounds of their power spectra are hard to model due to the oscillations being close to the Nyquist frequency.

By removing the underlying contributions from luminosity, mass and temperature (Kjeldsen & Bedding 2011), the significant metallicity influence stands out clearly as shown in Figure 12b, where metal-rich stars oscillate with larger amplitudes than metal-poor stars. The fitted values and the corresponding uncertainties of the parameters are shown in Table 3. The fitted scaling factor $\alpha = 2.02$ is different from unity, consistent with the results by Corsaro et al. (2017).

We repeated the fit on the HeB stars. The red clump and secondary clump stars in our sample differ significantly in metallicity. The former covers a much larger metallicity range than the latter, which are overall more metal rich. Considering our primary goal of investigating metallicity effects, we excluded secondary clump stars using a threshold $\nu_{\max} > 50 \mu\text{Hz}$. Figure 12d shows the metallicity influence also exists for red clump stars, where metal-rich stars again oscillate with higher amplitudes at given ν_{\max} , $\Delta\nu$, and T_{eff} .

We note that the oscillation amplitudes of RGB and red clump stars have different levels of dependence on ν_{\max} , $\Delta\nu$, and temperature, as the two relations show in Figure 12. The influences of ν_{\max} , $\Delta\nu$, and temperature on RGB stars are more significant than on red clump stars, as revealed by the globally larger absolute exponents of the relation for RGB stars than red clump stars (see Table 3). The different influence is because

ν_{\max} , $\Delta\nu$, and temperatures of RGB stars vary more significantly than for HeB stars.

Since the intensity fluctuation caused by granulation is related to the contrast between dark and bright regions of granules, the opacity and limb-darkening should have a strong effect on granulation power. Thus metallicity in turn might influence granulation power as well. Figure 13 displays the metallicity effect on granulation power measured at ν_{\max} , using the same model as shown in Equation 8. From Figure 13a, we observe that the metallicity effect is visible in the ν_{\max} range covered by secondary clump stars. With the attempt to remove underlying contributions from luminosity, mass, and temperature, Figure 13b indicates that the granulation power depends on metallicity, where metal-rich stars have larger granulation power than metal-poor stars.

Our results revealing the effect of metallicity on granulation power of field red giants are in agreement with the arguments given by Corsaro et al. (2017), who found that metallicity causes a statistically significant variation in the amplitude of the granulation activity of stars in the open clusters NGC 6791, NGC 6819, and NGC 6811. Collet et al. (2007) performed 3D hydrodynamical simulations of red giants with [Fe/H] from -3.0 through 0.0, and found that more metal-rich stars have larger granules (see their Figure 4) due to increased opacity. The increased horizontal size of a granule suggests metal-rich stars are expected to have greater granulation power, which is qualitatively consistent with our results. To understand this, we recall that a convection cell is usually assumed to travel a vertical distance proportional to the pressure scale height, H_p , at a speed scaling with the sound speed, c_s , thus the characteristic timescale of a granule can be expressed as $\tau_{\text{gran}} \propto H_p/c_s \propto (T_{\text{eff}}/g)/\sqrt{T_{\text{eff}}} \propto 1/\nu_{\max}$. The assumption of the horizontal size of a granule, d , proportional to the pressure scale height yields $d \propto H_p \propto T_{\text{eff}}/g \propto \sqrt{T_{\text{eff}}}/\nu_{\max}$. The proportionality of granulation power

Table 3. Fitted model parameters of oscillation amplitude and granulation power

Parameters	phase	α	β	γ	δ
Oscil. amp.	RGB	2.02 \pm 0.02	-2.85 \pm 0.04	2.95 \pm 0.05	-1.82 \pm 0.05
	Red clump	0.36 \pm 0.03	-1.99 \pm 0.02	1.36 \pm 0.04	-1.23 \pm 0.05
Gran. power	Red giants	0.38 \pm 0.01	-4.38 \pm 0.01	2.67 \pm 0.03	-2.22 \pm 0.05

Notes: The fitted values and uncertainties of the parameters, namely $\alpha, \beta, \gamma, \delta$, as defined in Equation 8. The oscillation amplitudes of RGB and red clump stars were fitted separately, while the granulation power of all red giants was fitted to the entire sample.

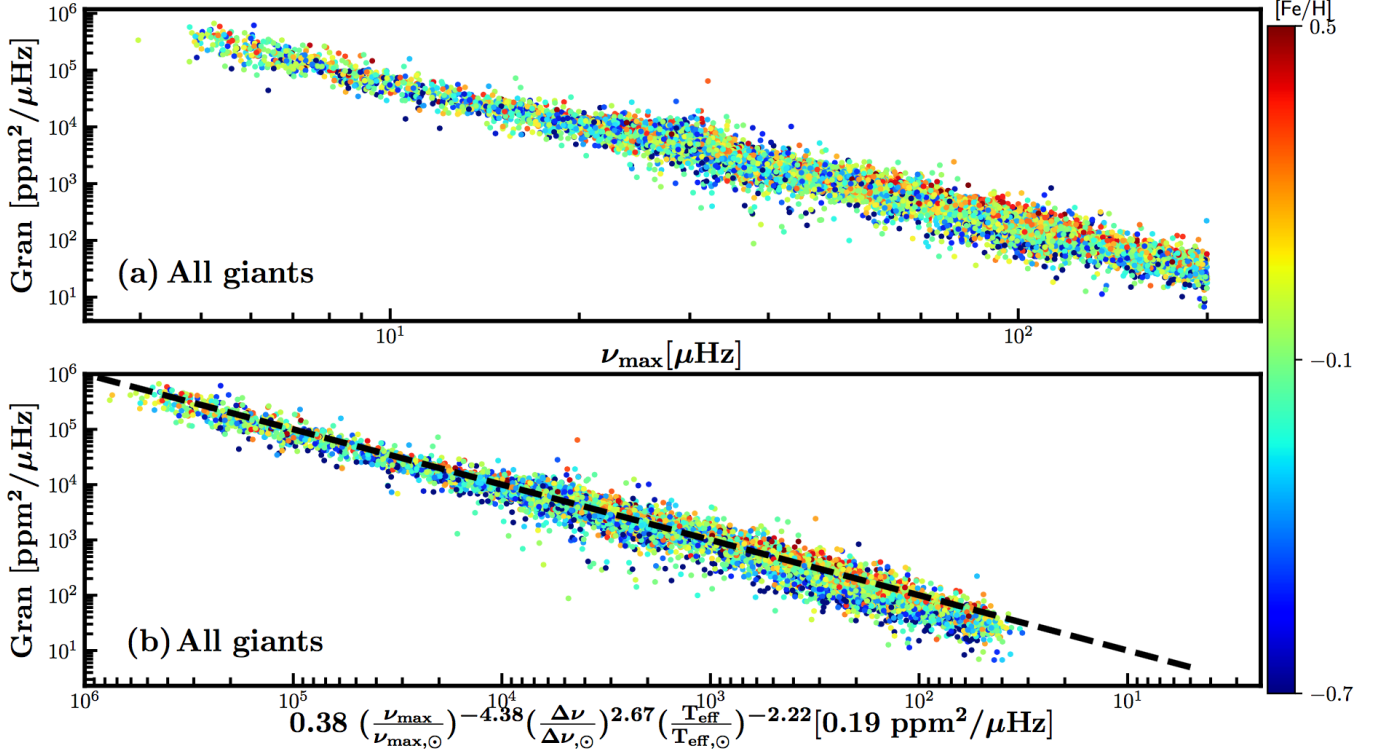


Figure 13. Similar to Figure 12 but for granulation power of all the red giants.

to $\sigma^2 \tau_{\text{gran}}$, with σ being the rms intensity fluctuation and varying much less than τ_{gran} , gives the granulation power $\text{Gran} \propto d/\sqrt{T_{\text{eff}}}$, hence, larger granules are expected to have larger granulation power (for more detail see Kjeldsen & Bedding 2011; Mathur et al. 2011).

To quantitatively measure the impact of metallicity on the oscillation amplitude and granulation power, we plot their residuals, in the sense of the observed divided by the fitted quantity, as a function of $[\text{Fe}/\text{H}]$ in Figure 14. The magenta points are the mean values in each $[\text{Fe}/\text{H}]$ bin with a width of 0.1 dex. A linear fit is also shown with the red line. Clearly, the oscillation amplitude depends on metallicity, causing 15% variation across the metallicity range $-0.7 < [\text{Fe}/\text{H}] < 0.5$ for both RGB and red clump stars and so does granulation power but with 25% scatter for the whole sample.

Note that when investigating the metallicity influence, we used $[\text{Fe}/\text{H}]$ estimates from Mathur et al. (2017), of which 48% originate from the KIC. Pinsonneault et al. (2014) found the KIC metallicities show good agreement with those from APOGEE for red giant stars (see their Figure 14). We also performed the same analysis but only using spectroscopic metallicity from Mathur et al. (2017), and found that the metallicity influence remains significant, as shown in Figure 15.

5. CONCLUSIONS AND DISCUSSIONS

We have presented a homogeneous analysis of 16094 oscillating red giants observed by *Kepler* mission using all available end-of-mission long-cadence data sets. We provide a catalog of global seismic parameters and seismically-derived mass, radius, and therefore surface gravity for oscillators with $\nu_{\max} > 5 \mu\text{Hz}$. We have also systematically investigated the distribution of oscillation amplitude, granulation power, and width of power excess in RGB and HeB stars separately, and their dependencies on stellar mass and metallicity. The main results are summarized as follows:

- We provide a catalog of seismic mass and radius and global oscillation parameters. The typical (median) uncertainties are 1.6% for ν_{\max} , 0.6% for $\Delta\nu$, 4.7% for oscillation amplitude, 8.6% for granulation power, 8.8% for width of power excess, 7.8% for mass, 2.9% for radius, and 0.01 dex for $\log g$.
- We have improved the SYD pipeline to provide more accurate $\Delta\nu$ estimates, some of which were incorrectly measured to be $\Delta\nu \pm \delta\nu_{02}$. Our ν_{\max} and $\Delta\nu$ measurements are in good agreement with literature, displaying a median fractional residual of 0.2% and a scatter of 3.5% for ν_{\max} , and a median fractional residual of 0.01% and a scatter of 4.2% for $\Delta\nu$.

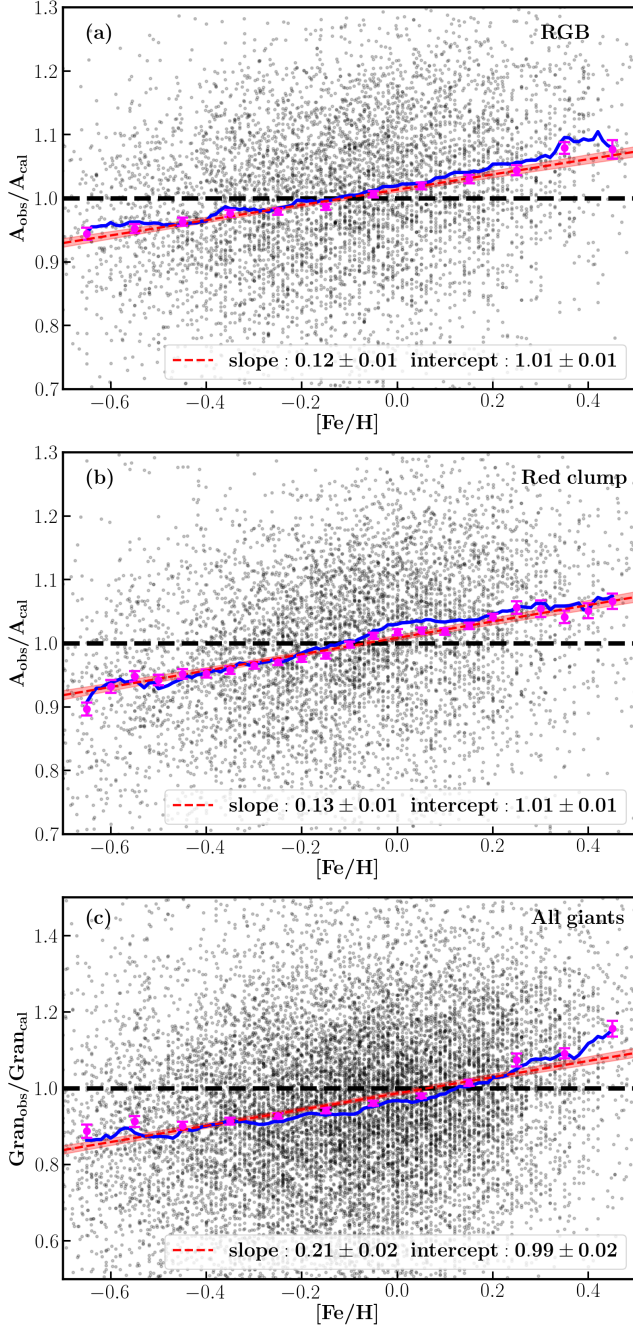


Figure 14. (a) The residual of the observed and predicted oscillation amplitude for RGB stars and (b) for red clump stars, and (c) the residual of the observed and predicted granulation power of red giants in the whole sample, as a function of $[\text{Fe}/\text{H}]$. A threshold of $\nu_{\text{max}} > 50 \mu\text{Hz}$ is used to separate red clump stars from secondary clump stars. In each panel, the blue line denotes the 50th percentiles of the residuals. The magenta points mark the mean residuals with error bars in each 1.0 dex wide bin. A linear fit to individual data points is shown by the red dashed line, with 95% confidence intervals in each box. The slopes and intercepts are indicated.

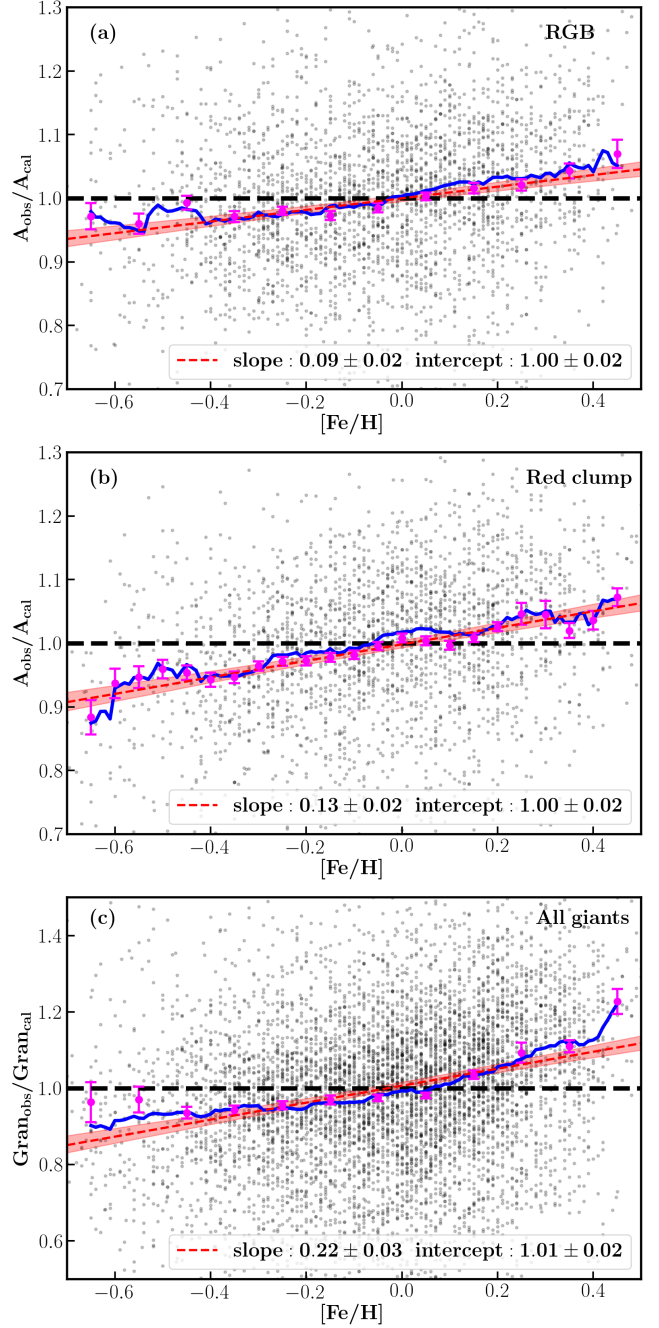


Figure 15. Similar as Figure 14 but only using spectroscopic $[\text{Fe}/\text{H}]$ from Mathur et al. (2017).

- We find that HeB stars form a extremely sharp edge as shown in Fig 7b, which we interpret as the zero-age main sequence for core helium-burning. We also find tentative evidence for mass loss at the RGB tip and AGB phase.
- RGB and HeB stars follow systematically different distributions of oscillation amplitude, power

excess width, and granulation power. Secondary clump stars have overall lower oscillation amplitude and granulation power, and broader power excess than RGB stars. This difference gradually attenuates towards lower- ν_{\max} RGB and HeB stars.

- The oscillation amplitude and granulation power have dependencies on mass and metallicity. We confirm that the width of power excess is an increasing function of mass. Metallicity has an influence on oscillation amplitude, leading to 15% variation for RGB stars and red clump stars in the metallicity range $-0.7 < [\text{Fe}/\text{H}] < 0.5$, and on granulation power, causing 25% spread for all the red giants in the sample. Metal-rich and lower-mass stars show larger oscillation amplitude and granulation power.

Given the difficulty in appropriately fitting power spectrum background, we do not report the measurement of oscillation amplitude, width of power excess, or granulation power for stars with $\nu_{\max} > 200 \mu\text{Hz}$. We excluded all the stars with $\nu_{\max} > 275 \mu\text{Hz}$, though measurements of $\Delta\nu$ using an autocorrelation function method is less affected (Yu et al. 2016).

Recently Mathur et al. (2017) delivered a characterization of stellar fundamental properties of *Kepler* targets for transit detection run. This is based on conditioning stellar atmospheric parameters on the isochrones from the Dartmouth Stellar Evolution Database, which does not include helium-burning models for low-mass stars. Our seismic determination of radius and mass are nearly independent of stellar models (except when correcting $\Delta\nu$) and therefore is able to remedy the bias of overestimated mass measurements for helium-core burning stars.

Our asteroseismic stellar properties can be used as reliable distance indicator and age proxies for mapping and dating the Galactic disk, as observed by the *Kepler* telescope. It is also useful to test and/or calibrate Gaia parallaxes. The precise and accurate seismically-derived surface gravities lift the degeneracies in spectroscopically deriving atmospheric parameters. The K2 and TESS missions are not expected to do seismology on stars that are as distant and faint as this sample, so these stars will remain benchmark red giants for many years to come.

Hon et al. (2017) have made use of our results for the successful classification of 5379 RGB and HeB stars. Wu et al. (2017) deduced ages of the RGB stars in our sample and applied them as a training data set to derive ages and masses directly from LAMOST spectra. Silva Aguirre et al. (2017) chemically dissected the Milky Way disk population using a sample of red giant stars with the asteroseismic ages, which were determined using the global oscillation parameters measured from this work.

Our sample does not include stars oscillating with ν_{\max} below $5 \mu\text{Hz}$. The scaling relations might not work appropriately because the low radial orders, n , of observed modes cannot be reliably approximated with an asymptotic theory. Thus the seismically-inferred stellar masses and radii would be biased. However, it is of significant interest to measure pulsation amplitudes and periods of those late RGB and AGB stars observed by *Kepler*. This would be a great sample to investigate the correlation between the amplitude and period for long-period variables (LPVs, Mosser et al. (2013b); Stello et al. (2014)) and their relation with mass loss (Yu et al. in prep.).

ACKNOWLEDGMENTS

The authors would like to thank our anonymous referee for a careful reading of our manuscript and many helpful comments. We also want to thank Hans Kjeldsen for fruitful discussions. We gratefully acknowledge the entire *Kepler* team and everyone involved in the *Kepler* mission for making this paper possible. Funding for the *Kepler* Mission is provided by NASA's Science Mission Directorate. Some/all of the data presented in this paper were obtained from the Mikulski Archive for Space Telescopes (MAST). STScI is operated by the Association of Universities for Research in Astronomy, Inc., under NASA contract NAS5-26555. Support for MAST for non-Hubble Space Telescope data is provided by the NASA Office of Space Science via grant NNX09AF08G and by other grants and contracts. D.H. acknowledges support by the Australian Research Council's Discovery Projects funding scheme (project number DE140101364) and support by the National Aeronautics and Space Administration under Grant NNX14AB92G issued through the Kepler Participating Scientist Program. D.S. is the recipient of an Australian Research Council Future Fellowship (project number FT1400147).

REFERENCES

- Alam, S., Albareti, F. D., Allende Prieto, C., et al. 2015, ApJS, 219, 12
 Bastien, F. A., Stassun, K. G., Basri, G., & Pepper, J. 2013, Nature, 500, 427

- Batalha, N. M., Borucki, W. J., Koch, D. G., et al. 2010, *ApJL*, 713, L109
- Beck, P. G., Montalban, J., Kallinger, T., et al. 2012, *Nature*, 481, 55
- Bedding, T. R., Kjeldsen, H., Campante, T. L., et al. 2010, *ApJ*, 713, 935
- Bedding, T. R., Mosser, B., Huber, D., et al. 2011, *Nature*, 471, 608
- Belkacem, K., Goupil, M. J., Dupret, M. A., et al. 2011, *A&A*, 530, A142
- Borucki, W. J., Koch, D., Basri, G., et al. 2010, *Science*, 327, 977
- Brogaard, K., VandenBerg, D. A., Bruntt, H., et al. 2012, *A&A*, 543, A106
- Brown, T. M., Gilliland, R. L., Noyes, R. W., & Ramsey, L. W. 1991, *ApJ*, 368, 599
- Brown, T. M., Latham, D. W., Everett, M. E., & Esquerdo, G. A. 2011, *AJ*, 142, 112
- Bruntt, H., Basu, S., Smalley, B., et al. 2012, *MNRAS*, 423, 122
- Casagrande, L., Silva Aguirre, V., Schlesinger, K. J., et al. 2016, *MNRAS*, 455, 987
- Cassisi, S., Castellani, V., Degl'Innocenti, S., Piotto, G., & Salaris, M. 2001, *A&A*, 366, 578
- Chaplin, W. J., Elsworth, Y., Davies, G. R., et al. 2014a, *MNRAS*, 445, 946
- Chaplin, W. J., Basu, S., Huber, D., et al. 2014b, *ApJS*, 210, 1
- Collet, R., Asplund, M., & Trampedach, R. 2007, *A&A*, 469, 687
- Corsaro, E., De Ridder, J., & García, R. A. 2015, *A&A*, 579, A83
- Corsaro, E., Fröhlich, H.-E., Bonanno, A., et al. 2013, *MNRAS*, 430, 2313
- Corsaro, E., Mathur, S., García, R. A., et al. 2017, *A&A*, 605, A3
- De Ridder, J., Barban, C., Baudin, F., et al. 2009, *Nature*, 459, 398
- Deheuvels, S., García, R. A., Chaplin, W. J., et al. 2012, *ApJ*, 756, 19
- Deheuvels, S., Doğan, G., Goupil, M. J., et al. 2014, *A&A*, 564, A27
- di Mauro, M. P., Cardini, D., Catanzaro, G., et al. 2011, *MNRAS*, 415, 3783
- Di Mauro, M. P., Ventura, R., Cardini, D., et al. 2016, *ApJ*, 817, 65
- Elsworth, Y., Hekker, S., Basu, S., & Davies, G. R. 2017, *MNRAS*, 466, 3344
- Fröhlich, C., Andersen, B. N., Appourchaux, T., et al. 1997, *SoPh*, 170, 1
- Fuller, J., Cantiello, M., Stello, D., Garcia, R. A., & Bildsten, L. 2015, *Science*, 350, 423
- García, R. A., Hekker, S., Stello, D., et al. 2011, *MNRAS*, 414, L6
- García, R. A., Pérez Hernández, F., Benomar, O., et al. 2014, *A&A*, 563, A84
- Gaulme, P., McKeever, J., Jackiewicz, J., et al. 2016, *ApJ*, 832, 121
- Gilliland, R. L. 2008, *AJ*, 136, 566
- Gilliland, R. L., Jenkins, J. M., Borucki, W. J., et al. 2010, *ApJL*, 713, L160
- Gough, D. O. 1986, in *Hydrodynamic and Magnetodynamic Problems in the Sun and Stars*, ed. Y. Osaki (Uni. of Tokyo Press), 117
- Guggenberger, E., Hekker, S., Angelou, G. C., Basu, S., & Bellinger, E. P. 2017, *MNRAS*, 470, 2069
- Guggenberger, E., Hekker, S., Basu, S., & Bellinger, E. 2016, *MNRAS*, 460, 4277
- Hekker, S., Elsworth, Y., Basu, S., et al. 2013a, *MNRAS*, 434, 1668
- Hekker, S., Elsworth, Y., Mosser, B., et al. 2013b, *A&A*, 556, A59
- Hekker, S., Kallinger, T., Baudin, F., et al. 2009, *A&A*, 506, 465
- Hekker, S., Gilliland, R. L., Elsworth, Y., et al. 2011a, *MNRAS*, 414, 2594
- Hekker, S., Elsworth, Y., De Ridder, J., et al. 2011b, *A&A*, 525, A131
- Hekker, S., Elsworth, Y., Mosser, B., et al. 2012, *A&A*, 544, A90
- Hon, M., Stello, D., & Yu, J. 2017, *MNRAS*, 469, 4578
- Huber, D., Stello, D., Bedding, T. R., et al. 2009, *Communications in Asteroseismology*, 160, 74
- Huber, D., Bedding, T. R., Stello, D., et al. 2010, *ApJ*, 723, 1607
- . 2011a, *ApJ*, 743, 143
- Huber, D., Bedding, T. R., Arentoft, T., et al. 2011b, *ApJ*, 731, 94
- Huber, D., Ireland, M. J., Bedding, T. R., et al. 2012, *MNRAS*, 423, L16
- Huber, D., Carter, J. A., Barbieri, M., et al. 2013a, *Science*, 342, 331
- Huber, D., Chaplin, W. J., Christensen-Dalsgaard, J., et al. 2013b, *ApJ*, 767, 127
- Huber, D., Silva Aguirre, V., Matthews, J. M., et al. 2014, *ApJS*, 211, 2
- Huber, D., Zinn, J., Bojsen-Hansen, M., et al. 2017, *ApJ*, 844, 102
- Kallinger, T., Hekker, S., Garcia, R. A., Huber, D., & Matthews, J. M. 2016, *Science Advances*, 2, 1500654

- Kallinger, T., Guenther, D. B., Matthews, J. M., et al. 2008, A&A, 478, 497
- Kallinger, T., Weiss, W. W., Barban, C., et al. 2010a, A&A, 509, A77
- Kallinger, T., Mosser, B., Hekker, S., et al. 2010b, A&A, 522, A1
- Kallinger, T., De Ridder, J., Hekker, S., et al. 2014, A&A, 570, A41
- Kjeldsen, H., & Bedding, T. R. 1995, A&A, 293, 87
- . 2011, A&A, 529, L8
- Kjeldsen, H., Bedding, T. R., Arentoft, T., et al. 2008, ApJ, 682, 1370
- Koch, D. G., Borucki, W. J., Basri, G., et al. 2010, ApJL, 713, L79
- Li, T., Bedding, T. R., Huber, D., et al. 2018, MNRAS, 475, 981
- Mathur, S., García, R. A., Huber, D., et al. 2016, ApJ, 827, 50
- Mathur, S., Hekker, S., Trampedach, R., et al. 2011, ApJ, 741, 119
- Mathur, S., Huber, D., Batalha, N. M., et al. 2017, ApJS, 229, 30
- Michel, E., Baglin, A., Auvergne, M., et al. 2008, Science, 322, 558
- Miglio, A. 2012, *Astrophysics and Space Science Proceedings*, 26, 11
- Miglio, A., Brogaard, K., Stello, D., et al. 2012, MNRAS, 419, 2077
- Miglio, A., Chiappini, C., Morel, T., et al. 2013, in *European Physical Journal Web of Conferences*, Vol. 43, European Physical Journal Web of Conferences, 3004, DOI: 10.1051/epjconf/20134303004
- Mosser, B., Vrard, M., Belkacem, K., Deheuvels, S., & Goupil, M. J. 2015, A&A, 584, A50
- Mosser, B., Belkacem, K., Goupil, M.-J., et al. 2010, A&A, 517, A22
- Mosser, B., Elsworth, Y., Hekker, S., et al. 2012a, A&A, 537, A30
- Mosser, B., Goupil, M. J., Belkacem, K., et al. 2012b, A&A, 548, A10
- Mosser, B., Michel, E., Belkacem, K., et al. 2013a, A&A, 550, A126
- Mosser, B., Dziembowski, W. A., Belkacem, K., et al. 2013b, A&A, 559, A137
- Mosser, B., Benomar, O., Belkacem, K., et al. 2014, A&A, 572, L5
- Mosser, B., Belkacem, K., Pinçon, C., et al. 2017, A&A, 598, A62
- Murphy, S. J. 2012, MNRAS, 422, 665
- Murphy, S. J., Shibahashi, H., & Kurtz, D. W. 2013, MNRAS, 430, 2986
- Pinsonneault, M. H., An, D., Molenda-Żakowicz, J., et al. 2012, ApJS, 199, 30
- Pinsonneault, M. H., Elsworth, Y., Epstein, C., et al. 2014, ApJS, 215, 19
- Quinn, S. N., White, T. R., Latham, D. W., et al. 2015, ApJ, 803, 49
- Schonhut-Stasik, J. S., Baranec, C., Huber, D., et al. 2017, ApJ, 847, 97
- Sharma, S., Stello, D., Bland-Hawthorn, J., Huber, D., & Bedding, T. R. 2016, ApJ, 822, 15
- Silva Aguirre, V., Casagrande, L., Basu, S., et al. 2012, ApJ, 757, 99
- Silva Aguirre, V., Bojsen-Hansen, M., Slumstrup, D., et al. 2017, ArXiv e-prints, arXiv:1710.09847
- Stello, D., Bruntt, H., Preston, H., & Buzasi, D. 2008, ApJL, 674, L53
- Stello, D., Cantiello, M., Fuller, J., et al. 2016, Nature, 529, 364
- Stello, D., Chaplin, W. J., Basu, S., Elsworth, Y., & Bedding, T. R. 2009, MNRAS, 400, L80
- Stello, D., & Gilliland, R. L. 2009, ApJ, 700, 949
- Stello, D., Huber, D., Kallinger, T., et al. 2011, ApJL, 737, L10
- Stello, D., Huber, D., Bedding, T. R., et al. 2013, ApJL, 765, L41
- Stello, D., Compton, D. L., Bedding, T. R., et al. 2014, ApJL, 788, L10
- Stello, D., Huber, D., Sharma, S., et al. 2015, ApJL, 809, L3
- Tassoul, M. 1980, ApJS, 43, 469
- Ulrich, R. K. 1986, ApJL, 306, L37
- Valenti, J. A., & Fischer, D. A. 2005, ApJS, 159, 141
- Verner, G. A., Elsworth, Y., Chaplin, W. J., et al. 2011, MNRAS, 415, 3539
- Vrard, M., Mosser, B., & Samadi, R. 2016, A&A, 588, A87
- White, T. R., Bedding, T. R., Stello, D., et al. 2011, ApJ, 743, 161
- White, T. R., Huber, D., Maestro, V., et al. 2013, MNRAS, 433, 1262
- Wu, Y., Xiang, M., Bi, S., et al. 2017, ArXiv e-prints, arXiv:1712.09779
- Yıldız, M., Çelik Orhan, Z., & Kayhan, C. 2016, MNRAS, 462, 1577
- Yu, J., Huber, D., Bedding, T. R., et al. 2016, MNRAS, 463, 1297
- Ziegler, C., Law, N. M., Morton, T., et al. 2017, AJ, 153, 66